

BY Y. MISHCHENKO L. PANINSKI J. VOGELSTEIN

## A BAYESIAN APPROACH TO INFERRING FUNCTIONAL CONNECTIVITY GIVEN POPULATION CALCIUM IMAGING

**1. Introduction.** Since Ramon y Cajal discovered that the brain is a rich and dense *network* of neurons (Ramon y Cajal, 1904; Ramon y Cajal, 1923), neuroscientists have been intensely curious about the details of these networks, which are believed to be the biological substrate for memory, cognition, and perception. While we have learned a great deal in the last century about “macro-circuits” — the connectivity between coarsely-defined brain areas — relatively little is known about “micro-circuits,” i.e., the connectivity within populations of neurons at a fine-grained cellular level. One can imagine two complementary strategies for inferring microcircuit connectivity: anatomical and functional. Anatomical approaches to inferring circuitry include, for example, recently developed technologies of array tomography (Micheva and Smith, 2007), “brainbow” mice (Livet et al., 2007), and serial electron microscopy (Briggman and Denk, 2006). Our work, on the other hand, takes a functional approach: our aim is to infer microcircuit properties by observing the activity of a population of neurons.

Experimental tools that enable approximately simultaneous observations of the activity of many (e.g.,  $O(10^3)$ ) neurons are now widely available. While arrays of extracellular electrodes have been exploited for this purpose, the arrays most often used *in vivo* are inadequate for inferring monosynaptic connectivity in very large populations of neurons, as the inter-electrode spacing is typically too large to record from all of the neurons in a given volume, and technologically possible number of electrodes in the arrays limits the number of neurons that can be simultaneously observed (Hatsopoulos et al., 1998; Harris et al., 2003; Stein et al., 2004; Santhanam et al., 2006; Luczak et al., 2007)<sup>1</sup>. Alternately, calcium-sensitive fluorescent indicators allow us to observe the spiking activity of  $\sim 10,000$  neighboring neurons (Tsien, 1989), which are more likely to be connected (Abeles, 1991; Braitenberg and Schuz, 1998). Some organic dyes achieve sufficiently high signal-to-noise ratios (SNR) that individual action potentials (spikes) may be resolved (Yuste et al., 2006), and bulk-loading techniques enable experimentalists to simultaneously fill populations of neurons with such dyes (Stosiek et al., 2003). In addition, genetically encoded calcium indicators are under rapid development in a number of groups, and are approaching SNR levels of nearly single spike accuracy as well (Wallace et al., 2008). Microscopy technologies for collecting fluorescence signals are also rapidly developing. Cooled CCDs for wide-field imaging (either epifluorescence or confocal) now achieve a quantum efficiency of  $\approx 90\%$  with frame rates up to 60 Hz or greater, depending on the width of the field of view (Djurisic et al., 2004). For *in vivo* work, 2-photon laser scanning microscopy can achieve similar frame rates, using acoustic-optical deflectors to focus light at arbitrary locations in three-dimensional space (Reddy and Saggau, 2005; Iyer et al., 2006; Salome et al., 2006; Reddy et al., 2008), or using resonant scanners (Nguyen et al., 2001). Together, these experimental tools can provide movies of calcium fluorescence transients for small populations of neurons (e.g.,  $O(10^2)$ ) with “reasonable” SNR, and at imaging frequencies of 30 Hz or greater, in both the *in vitro* and *in vivo* settings.

---

<sup>1</sup>It is worth noting, however, that multielectrode arrays which have been recently developed for use in the retina are capable of much denser sampling (Segev et al., 2004; Litke et al., 2004; Petrusca et al., 2007; Pillow et al., 2008).

Given these experimental advances in functional neural imaging, our goal is to develop efficient computational and statistical methods to exploit this data for the analysis of neural connectivity. See Fig. 3 for a schematic overview. One major challenge here is that calcium transients due to action potentials provide indirect observation of the neural activity, and decay about an order of magnitude slower than the time course of the underlying neural activity (Yuste et al., 2006). Thus, to properly analyze the functional network connectivity, we must incorporate a method for effectively deconvolving the observed noisy fluorescence signal to obtain estimates of the underlying spiking rates (Yaksi and Friedrich, 2006; Greenberg et al., 2008; Vogelstein et al., 2009). To this end we introduce a coupled Markovian state-space model that relates the observed variables (fluorescence traces from the neurons in the microscope’s field of view) to the hidden variables (spike trains and intracellular calcium concentrations of these neurons), as governed by a set of biophysical parameters including the network connectivity matrix. Given this model, we derive a Monte Carlo Expectation Maximization algorithm for obtaining the maximum a posteriori estimates of the parameters of interest. Standard Monte Carlo sampling procedures (e.g., Gibbs sampling or sequential Monte Carlo) are inadequate in this setting, due to the high dimensionality and non-linear, non-Gaussian dynamics of the hidden variables in our model; we therefore develop a specialized blockwise-Gibbs approach to overcome these obstacles. This strategy enables us to accurately infer the functional connectivity matrix from large simulated neural populations, under realistic assumptions about the dynamics and observation parameters. We describe our approach below, along with several methods for improving its computational speed and statistical efficiency.

## 2. Methods. (0)

**2.1. Model.** We begin by detailing a parametric generative model for the (unobserved) joint spike trains of all  $N$  observable neurons, along with the observed calcium fluorescence data. Each neuron is modeled as a generalized linear model (GLM). This class of model is known to capture the statistical firing properties of individual neurons fairly accurately (Brillinger, 1988; Chornoboy et al., 1988; Brillinger, 1992; Plesser and Gerstner, 2000; Pillow et al., 2008; Paninski et al., 2004; Paninski, 2004; Rigat et al., 2006; Truccolo et al., 2005; Nykamp, 2007; Kulkarni and Paninski, 2007; Vidne et al., 2009; Stevenson et al., 2009). We denote the  $i$ -th neuron’s activity at time  $t$  as  $n_i(t)$ : in continuous time,  $n_i(t)$  could be modeled as an unmarked point process, but we will take a discrete-time approach here, with each  $n_i(t)$  taken to be a binary random variable. We model the spiking probability of neuron  $i$  via an instantaneous nonlinear function,  $f(\cdot)$ , of the filtered and summed input to that neuron at that time,  $J_i(t)$ . This input is composed of: (i) some baseline value,  $b_i$ ; (ii) some external vector stimulus,  $S^{ext}(t)$ , that is linearly filtered by  $k_i$ ; and (iii) spike history terms,  $h_{ij}(t)$ , encoding the influence on neuron  $i$  from neuron  $j$ , weighted by  $w_{ij}$ :

$$(1) \quad n_i(t) \sim \text{Bernoulli}[f(J_i(t))], \quad J_i(t) = b_i + k_i \cdot S^{ext}(t) + \sum_{j=1}^N w_{ij} h_{ij}(t).$$

To ensure computational tractability of the parameters inference problem, we must impose some reasonable constraints on the instantaneous nonlinearity  $f(\cdot)$  (which plays the role of the inverse of the link function in the standard GLM setting) and on the dynamics of the spike-history effects  $h_{ij}(t)$ . First, we restrict our attention to functions  $f(\cdot)$  which ensure the

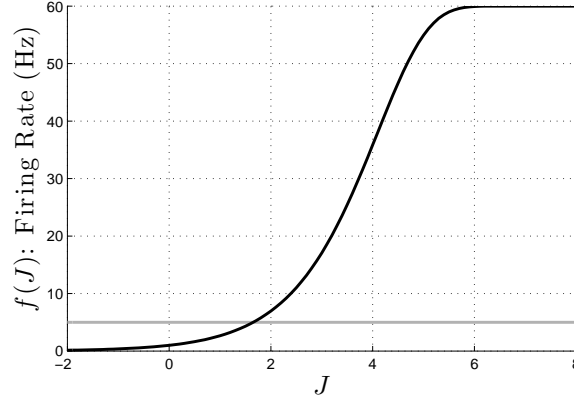


FIG 1. A plot of the firing rate nonlinearity  $f(J)$  used in our simulations. Note that the firing rate saturates at  $1/\Delta$ , because of our Bernoulli assumption (i.e., the spike count per bin is at most one). Here  $\Delta = (60 \text{ Hz})^{-1}$ .

concavity of the spiking loglikelihood in this model (Paninski, 2004; Escola and Paninski, 2008), as we will discuss at more length below. In this paper, we use

$$(2) \quad f(J) = P[n > 0 \mid n \sim \text{Pois}(e^J \Delta)] = 1 - \exp[-e^J \Delta]$$

(Fig. 1), where the inclusion of  $\Delta$ , the time step size, ensures that the firing rate scales properly with respect to the time discretization; see (Escola and Paninski, 2008) for a proof that this  $f(\cdot)$  satisfies the required concavity constraints. However, we should note that in our experience the results depend only weakly on the details of  $f(\cdot)$  within the class of log-concave models (Li and Duan, 1989; Paninski, 2004).

Second, because the algorithms we develop below assume Markovian dynamics, we model the spike history terms as an autoregressive process:

$$(3) \quad h_{ij}(t) = (1 - \Delta/\tau_{ij}^h)h_{ij}(t - \Delta) + n_j(t) + \sigma_{ij}^h \sqrt{\Delta} \epsilon_{ij}^h(t),$$

where  $\tau_{ij}^h$  is the decay time constant for spike history terms,  $\sigma_{ij}^h$  is a standard deviation parameter,  $\sqrt{\Delta}$  ensures that the statistics of this Markov process have a proper Ornstein-Uhlenbeck limit as  $\Delta \rightarrow 0$ , and throughout this paper,  $\epsilon$  denotes an independent standard normal random variable. Note that this model generalizes (via a simple augmentation of the state variable  $h_{ij}(t)$ ) to allow each neuron to have several spike history terms, each with a unique time constant, which when weighted and summed allow us to model a wide variety of possible post-synaptic effects, including bursting, facilitating, and depressing synapses; see (Vogelstein et al., 2009) for further details. We restrict our attention to the case of a single time constant  $\tau_{ij}^h$  here, so the deterministic part of  $h_{ij}(t)$  is a simple exponential function. Furthermore, we assume that  $\tau_{ij}^h$  is the same for all neurons and all synapses, although in principle each synapse could be modeled with its unique  $\tau_{ij}^h$ . We do that both for simplicity and also because we find that the detailed shape of the coupling terms  $h_{ij}(t)$  had a limited effect on the inference of the connectivity matrix, as illustrated in Fig. 12 below. Thus, we treat  $\tau_{ij}^h$  and  $\sigma_{ij}^h$  as known synaptic parameters which are the same for each neuron pair  $(i, j)$ ; therefore our unknown model spiking parameters are  $\{\mathbf{w}_i, k_i, b_i\}_{i \leq N}$ , with  $\mathbf{w}_i = (w_{i1}, \dots, w_{iN})$ .

The problem of estimating the connectivity parameters  $\mathbf{w}_i$  in this type of GLM, given a fully-observed ensemble of neural spike train  $\{n_i(t)\}_{i \leq N}$ , has recently received a great deal

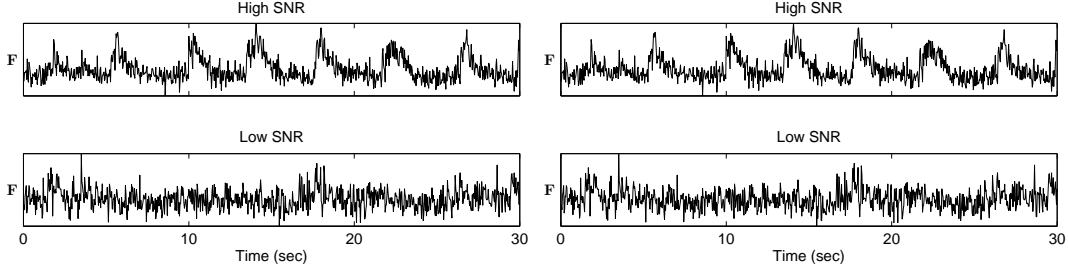


FIG 2. *I'm gonna modify this fig, to show 2 traces with spikes recorded using e-phys as well, show inferred calcium too maybe (superimposed on fluorescence). this seems like the "right" thing to do here, to convince the reader that our model is good. I'll explain in the caption how the parameters were estimated (using the true spikes), to get photon budget.*

of attention; see the references above for a partial list. In the calcium fluorescent imaging setting, however, we do not directly observe spike trains;  $\{n_i(t)\}_{i \leq N}$  must be considered a hidden variable here. Instead, each spike in a given neuron leads to a rapid increase in the intracellular calcium concentration, which then decays slowly due to various cellular buffering and extrusion mechanisms. We in turn make only noisy, indirect, and subsampled observations of this intracellular calcium concentration, via fluorescent imaging techniques (Yuste et al., 2006). To perform statistical inference in this setting, (Vogelstein et al., 2009) proposed a simple conditional first-order hidden Markov model (HMM) for the intracellular calcium concentration  $C_i(t)$  in cell  $i$  at time  $t$ , along with the observed fluorescence  $F_i(t)$ :

$$(4) \quad C_i(t) = C_i(t - \Delta) + (C_i^b - C_i(t - \Delta))\Delta/\tau_i^c + A_i n_i(t) + \sigma_i^c \sqrt{\Delta} \epsilon_i^c(t),$$

$$(5) \quad F_i(t) = \alpha_i S(C_i(t)) + \beta_i + \sqrt{\gamma_i S(C_i(t))} \epsilon_i^F(t).$$

This model can be interpreted as a simple driven autoregressive process: under nonspiking conditions,  $C_i(t)$  fluctuates around the baseline level of  $C_i^b$ , driven by normally-distributed noise  $\epsilon_i^c(t)$  with standard deviation  $\sigma_i^c \sqrt{\Delta}$ . Whenever the neuron fires a spike,  $n_i(t) = 1$ , the calcium variable  $C_i(t)$  jumps by a fixed amount  $A_i$ , and subsequently decays with time constant  $\tau_i^c$ . The fluorescence signal  $F_i(t)$  corresponds to the count of photons collected at the detector per neuron per imaging frame. This photon count may be modeled with normal statistics, with the mean given by a scaled and shifted Hill function  $S(C) = C/(C + K_d)$  (Yasuda et al., 2004) and the variance proportional to the mean (which follows from assuming the Poisson statistics of the photon counts are well approximated with Normal distribution; see (Vogelstein et al., 2009) for further discussion. Because the parameter  $K_d$  effectively acts as a simple scale factor, and is a property of the fluorescent indicator, we assume throughout this work that it is known. Figure 2 shows that this calcium-observation model, Eqs. (4) – (5), captures the statistics of calcium imaging well.

To summarize, Eqs. (1) – (5) define a coupled HMM: the underlying spike trains  $n_i(t)$  and spike history terms  $h_{ij}(t)$  evolve in a Markovian manner given the stimulus  $S^{ext}(t)$ . These spike trains in turn drive the intracellular calcium concentrations  $C_i(t)$ , which are themselves Markovian, but evolving at a slower timescale  $\tau_i^c$ . Finally, we observe only the fluorescence signals  $\{F_i(t)\}_{i \leq N}$ , which are related in a simple Markovian fashion to the calcium variables  $C_i(t)$ .

**2.2. Goal and general strategy.** Our primary goal is to estimate the connectivity matrix,  $\mathbf{w}$ , given the observed set of calcium fluorescence signals  $\mathbf{F}^2$ . We must also deal with a number of nuisance parameters,  $\tilde{\theta}_i$ : the intrinsic dynamics parameters  $\{k_i, b_i, w_{ii}\}_{i \leq N}$ , the calcium parameters  $\{C_i^b, \tau_i^c, A_i, \sigma_i^c\}_{i \leq N}$ , and the observation parameters  $\{\alpha_i, \beta_i, \gamma_i, \sigma_i^F\}_{i \leq N}$ . We addressed the problem of estimating these latter parameters in earlier work (Vogelstein et al., 2009); thus our focus here will be on the connectivity matrix  $\mathbf{w}$ . A Bayesian approach is natural here, since we have a good deal of prior information about neural connectivity; see (Rigat et al., 2006) for a related discussion. However, a fully-Bayesian approach, in which we numerically integrate over the very high-dimensional parameters' space  $\theta = \{\theta_i\}_{i \leq N}$  — where  $\theta_i = \{\mathbf{w}_i, k_i, b_i, C_i^b, \tau_i^c, A_i, \sigma_i^c, \alpha_i, \beta_i, \gamma_i, \sigma_i^F\}$ , and the nuisance parameters for neuron  $i$  are all its parameters, minus the cross-coupling terms, i.e.  $\tilde{\theta}_i = \theta_i \setminus \{w_{ij}\}_{i \neq j}$  — is not particularly attractive from a computational point of view. Thus, our compromise is to compute *maximum a posteriori* (MAP) estimates for the parameters via an expectation-maximization (EM) algorithm in which the sufficient statistics are computed by a hybrid blockwise Gibbs sampler and sequential Monte Carlo (SMC) method.

More specifically, we iterate the steps:

**E step:** Evaluate  $Q(\theta, \theta^{(l)}) = E_{P[\mathbf{X}|\mathbf{F}, \theta^{(l)}]} \ln P[\mathbf{F}, \mathbf{X}|\theta] = \int P[\mathbf{X}|\mathbf{F}; \theta^{(l)}] \ln P[\mathbf{F}, \mathbf{X}|\theta] d\mathbf{X}$

**M step:** Solve  $\theta^{(l+1)} = \underset{\theta}{\operatorname{argmax}} \left\{ Q(\theta, \theta^{(l)}) + \ln P(\theta) \right\}$ ,

where  $\mathbf{X}$  denotes the set of all hidden variables  $\{C_i(t), n_i(t), h_{ij}(t)\}_{i,j \leq N, t \leq T}$  and  $P(\theta)$  denotes a (possibly improper) prior on the parameter space  $\theta$ . According to standard EM theory (Dempster et al., 1977; McLachlan and Krishnan, 1996), each iteration of these two steps is guaranteed to increase the log-posterior  $\ln P(\theta^{(l)}|\mathbf{F})$ , and will therefore lead to at least a locally maximum a posteriori estimator.

Now, our major challenge is to evaluate the auxiliary function  $Q(\theta, \theta^{(l)})$  in the E-step. Our model is a coupled HMM, as discussed in the previous section; therefore, as usual in the HMM setting (Rabiner, 1989),  $Q$  may be broken up into a sum of simpler terms:

$$\begin{aligned}
 Q(\theta, \theta^{(l)}) &= \sum_{it} P[C_i(t)|F_i; \tilde{\theta}_i] \times \ln P[F_i(t)|C_i(t); \alpha_i, \beta_i, \gamma_i, \sigma_i^F] \\
 &+ \sum_{it} P[C_i(t), C_i(t - \Delta), n_i(t)|F_i; \tilde{\theta}_i] \times \ln P[C_i(t)|C_i(t - \Delta), n_i(t); C_i^b, \tau_i^c, A_i, \sigma_i^c] \\
 (6) \quad &+ \sum_{it} P[n_i(t), \mathbf{h}_i(t)|\mathbf{F}; \theta_i] \times \ln P[n_i(t)|\mathbf{h}_i(t); b_i, k_i, \mathbf{w}_i, S^{ext}(t)],
 \end{aligned}$$

where  $\mathbf{h}_i(t) = \{h_{ij}(t)\}_{j \leq N}$ . Note that each of the three sums here corresponds to a different component of the model described in Eqs. (1) – (5): the first sum involves the fluorescent observation parameters, the second the calcium dynamics, and the third the spiking dynamics.

Thus we need only compute low-dimensional marginals of the full posterior distribution  $P[\mathbf{X}|\mathbf{F}; \theta]$ ; specifically, we need pairwise marginals, of the form  $P[C_i(t), C_i(t - \Delta)|F_i; \tilde{\theta}_i]$ , and marginals  $P[C_i(t)|F_i; \tilde{\theta}_i]$  and  $P[n_i(t), \mathbf{h}_i(t)|\mathbf{F}; \theta_i]$ . Calculation of marginals  $P[C_i(t), C_i(t - \Delta)|F_i; \tilde{\theta}_i]$  and marginals  $P[C_i(t)|F_i; \tilde{\theta}_i]$  is described in detail in (Vogelstein et al., 2009). Calculation of the joint marginal for high dimensional hidden variable  $\mathbf{h}_i$  necessitates the development of specialized blockwise Gibbs-SMC sampling method, as we describe in the subsequent

<sup>2</sup>Throughout this text, we abbreviate the entire state sequence,  $(X_1, \dots, X_T)$ , with  $X$ .

sections 2.3 and 2.4. Once we have obtained these marginals, the M-step breaks up into a number of independent optimizations that may be computed in parallel and which are therefore relatively straightforward (Section 2.5); see section 2.6 for a pseudocode summary along with some specific implementation details.

*2.3. Initialization of nuisance parameters via sequential Monte Carlo methods.* We begin by constructing relatively cheap, approximate preliminary estimators for the nuisance parameters  $\tilde{\theta}_i$ . The idea is to initialize our estimator by assuming that each neuron is observed independently. Thus we want to compute  $P[C_i(t), C_i(t - \Delta)|F_i; \tilde{\theta}_i]$  and  $P[C_i(t)|F_i; \tilde{\theta}_i]$ , and solve the M-step for each  $\tilde{\theta}_i$ , with the connectivity matrix parameters held fixed. This single-neuron case is much simpler, and has been discussed at length in (Vogelstein et al., 2009); therefore, we only provide a brief overview here. The standard forward and backward recursions provide these posteriors (Shumway and Stoffer, 2006):

(7)

$$P[X_i(t)|F_i(0:t)] \propto P[F_i(t)|X_i(t)] \int P[X_i(t)|X_i(t - \Delta)]P[X_i(t - \Delta)|F_i(0:t - \Delta)]dX_i(t - \Delta),$$

(8)

$$P[X_i(t), X_i(t - \Delta)|F_i] = P[X_i(t)|F_i] \frac{P[X_i(t)|X_i(t - \Delta)]P[X_i(t - \Delta)|F_i(0:t - \Delta)]}{\int P[X_i(t)|X_i(t - \Delta)]P[X_i(t - \Delta)|F_i(0:t - \Delta)]dX_i(t - \Delta)},$$

where  $F_i(s:t)$  denotes the time series  $F_i$  from time points  $s$  to  $t$ , and we have dropped the conditioning on the parameters  $\theta$  for brevity's sake. Eq. (7) describes the forward, or the filter, pass of the recursion, and Eq. (8) describes the backward, or smoother, pass, provides both  $P[X_i(t)|F_i]$  and  $P[X_i(t), X_i(t - \Delta)|F_i]$ .

Because these integrals cannot be analytically evaluated for our model, we approximate them using a SMC (“marginal particle filtering”) method (Doucet et al., 2000; Doucet et al., 2001; Godsill et al., 2004); see (Vogelstein et al., 2009) for details on the proposal density and resampling methods used here. The output of this SMC method comprises an array of particle positions  $\{X_i^{(m)}(t)\}_{m=1}^M$ , where  $m$  indexes the particle number, and a discrete approximation to the marginals  $P[X_i(t), X_i(t - \Delta)|F_i]$ ,

$$(9) \quad P[X_i(t), X_i(t - \Delta)|F_i] \approx \sum_{m, m'} r_i^{(m, m')}(t, t - \Delta) \delta[X_i(t) - X_i^{(m)}(t)] \delta[X_i(t - \Delta) - X_i^{(m')}(t - \Delta)],$$

where  $r_i^{(m, m')}(t, t - \Delta)$  denotes the weight attached to the pair of particles with positions  $(X_i^{(m)}(t), X_i^{(m')}(t - \Delta))$ , and  $\delta(\cdot)$  denotes a Dirac mass.

As discussed above, the sufficient statistics for estimating the nuisance parameters for each neuron,  $\tilde{\theta}_i$ , are exactly these marginal posteriors. As discussed following Eq. (6), the M-step decouples into three independent subproblems. The first term depends on only  $\{\alpha_i, \beta_i, \gamma_i, \sigma_i\}$ ; since  $\ln P[F_i(t)|C_i(t); \tilde{\theta}_i]$  is quadratic (by our Gaussian assumption on the fluorescent observation noise), we can estimate these parameters by solving a weighted regression problem (specifically, we use a coordinate-optimization approach: we solve a quadratic problem for  $\{\alpha_i, \beta_i\}$  while holding  $\{\gamma_i, \sigma_i\}$  fixed, then estimate  $\{\gamma_i, \sigma_i\}$  by the usual residual error formulas while holding  $\{\alpha_i, \beta_i\}$  fixed). Similarly, the second term requires us to optimize over

$\{\tau_i^c, A_i, C_i^b\}$ , and then we use the residuals to estimate  $\sigma_i^c$ . Note that all the parameters mentioned so far are constrained to be non-negative, but may be solved efficiently using standard quadratic program solvers if we use the simple reparameterization  $\tau_i^c \rightarrow 1 - \Delta/\tau_i^c$ . Finally, the last term, assuming neurons are independent, may be expanded:

$$(10) \quad E[\ln P[n_i(t), \mathbf{h}_i(t)|\mathbf{F}; \theta_i]] = \\ = P[n_i(t), \mathbf{h}_i(t)|\mathbf{F}] \ln f[J_i(t)] + (1 - P[n_i(t), \mathbf{h}_i(t)|\mathbf{F}]) \ln[1 - f(J_i(t))];$$

since  $J_i(t)$  is a linear function of  $\{b_i, k_i, \mathbf{w}_i\}$ , and the right-hand side of Eq. (10) is concave in  $J_i(t)$ , we see that the third term in Eq. (6) is a sum of terms which are concave in  $\{b_i, k_i, \mathbf{w}_i\}$  — and therefore also concave in the linear subspace  $\{b_i, k_i, w_{ii}\}$  with  $\{w_{ij}\}_{i \neq j}$  held fixed — and may thus be maximized efficiently using any convex optimization method, e.g. Newton-Raphson or conjugate gradient ascent.

Our procedure therefore is to initialize the parameters for each neuron using some default values that we have found to be practically effective in analyzing real data, and then recursively (i) estimate the marginal posteriors via Eq. (9) (E step), and (ii) maximize the nuisance parameters  $\tilde{\theta}_i$  (M step), using the above described approach. We iterate these two steps until the change in parameters  $\tilde{\theta}_i$  does not exceed some minimum threshold. We then use the marginal posteriors from the last iteration to seed the blockwise Gibbs sampling procedure described below. With that, we approximate  $P[n_i, \mathbf{h}_i|\mathbf{F}; \theta_i]$ .

*2.4. Estimating joint posteriors over weakly coupled neurons.* Now we turn to the key problem: constructing the sample from the joint marginal  $P[n_i(t), \mathbf{h}_i(t)|\mathbf{F}; \theta]$ , which encapsulates the sufficient statistics for estimating the connectivity matrix  $\mathbf{w}$  (recall Eq. (6)). The SMC method described in the preceding section only provide the marginals over each neuron; this method may in principle be extended to obtain the desired full posterior  $P[\mathbf{X}(t), \mathbf{X}(t - \Delta)|\mathbf{F}; \theta]$ , but the SMC is fundamentally a sequential importance sampling method, and therefore scales poorly as the dimensionality of the hidden state  $\mathbf{X}(t)$  increases (Bickel et al., 2008). Thus we need a different approach.

One very simple idea is to use a Gibbs sampler: sample sequentially from

$$(11) \quad X_i(t) \sim P[X_i(t)|\mathbf{X}_{\setminus i}, X_i(0), \dots, X_i(t - \Delta), X_i(t + \Delta), \dots, X_i(T), \mathbf{F}; \theta],$$

looping over all cells  $i$  and all time bins  $t$ . Unfortunately, this approach is likely to mix poorly, due to the strong temporal dependence between  $X_i(t)$  and  $X_i(t + \Delta)$ . Instead, we propose a blockwise Gibbs strategy, sampling one spike train as a block:

$$(12) \quad X_i \sim P[X_i|\mathbf{X}_{\setminus i}, \mathbf{F}; \theta].$$

If we can draw these blockwise samples  $X_i = X_i(0 : t)$  efficiently for a large subset of adjacent time-bins  $t$  simultaneously, then we would expect the resulting Markov chain to mix much more quickly than the single-element Gibbs chain, since by assumption the hidden variables  $X_i$  and  $X_j$  are weakly dependent for different cells  $i \neq j$ , and Gibbs is most efficient for weakly-dependent variables (Robert and Casella, 2005).

So, how can we efficiently sample from  $P[\mathbf{X}_i|\mathbf{X}_{\setminus i}, \mathbf{F}; \theta]$ ? One attractive approach is to try to re-purpose the SMC method described above, which is quite effective for drawing approximate samples from  $P[\mathbf{X}_i|\mathbf{X}_{\setminus i}, F_i; \theta]$  for one neuron  $i$  at a time. Recall that sampling from an HMM is in principle easy by the “propagate forward, sample backward” method: we first compute

the forward probabilities  $P[X_i(t)|\mathbf{X}_{\setminus i}(0:t), F_i(0:t); \theta]$  recursively for timesteps 0 up to  $T$ , then sample backwards from  $P[X_i(t)|\mathbf{X}_{\setminus i}(0:T), F_i(0:T), X_i(t+\Delta); \theta]$ . This approach is powerful because each sample requires just linear time to compute (i.e.,  $O(T/\Delta)$  time, where  $T/\Delta$  is the number of desired time steps). Unfortunately, in this case we can only compute the forward probabilities approximately (with the SMC forward recursion Eqn. (7)), and so therefore this attractive forward-backward approach only provides approximate samples from  $P[\mathbf{X}_i|\mathbf{X}_{\setminus i}, \mathbf{F}; \theta]$ , not the exact samples required for the validity of the Gibbs method.

Of course, in principle we should be able to use the Metropolis-Hastings (M-H) algorithm to correct these approximate samples. The problem is that the M-H acceptance ratio in this setting involves a high-dimensional integral over the set of paths that the particle filter might possibly trace out, and is therefore difficult to compute directly. (Andrieu et al., 2007) discuss this problem at more length, along with some proposed solutions. However, a slightly simpler approach was introduced by (Neal et al., 2003). Their idea is to exploit the  $O(T/\Delta)$  forward-backward sampling method by embedding a discrete Markov chain within the continuous state space  $\mathcal{X}_t$ ; the state space of this discrete embedded chain is sampled randomly according to some distribution  $\rho_t$  with support on  $\mathcal{X}_t$ . It turns out that an appropriate acceptance probability (defined in terms of the original state space model transition and observation probabilities, along with the auxiliary sampling distributions  $\rho_t$ ) may be computed quite tractably, guaranteeing that the samples produced by this algorithm form a Markov chain with the desired equilibrium density. See (Neal et al., 2003) for details.

We can apply this embedded-chain method quite directly here to sample from  $P[\mathbf{X}_i|\mathbf{X}_{\setminus i}, \mathbf{F}; \theta]$ . The one remaining question is how to choose the auxiliary densities  $\rho_t$ . We would like to choose these densities to be close to the desired marginal densities  $P[X_i(t)|\mathbf{X}_{\setminus i}, \mathbf{F}; \theta]$ , and conveniently, we have already computed a good (discrete) approximation to these densities, using the SMC methods described in the last section. The algorithm described in (Neal et al., 2003) requires that  $\rho_t$  be continuous densities, so we simply convolve our discrete SMC-based approximation (specifically, the  $X_i(t)$ -marginal of Eq. (9)) with an appropriate normal density to arrive at a very tractable mixture-of-Gaussians representation for  $\rho_t$  with required properties.

Thus, to summarize, our procedure for sampling from the desired joint state distributions  $P[n_i, \mathbf{h}_i|\mathbf{F}; \theta_i]$  has a Metropolis-within-blockwise-Gibbs flavor, where the internal Metropolis step is replaced by the  $O(T/\Delta)$  embedded-chain method introduced by (Neal et al., 2003), and the auxiliary densities  $\rho_t$  necessary for implementing the embedded-chain sampler are obtained using the SMC methods from (Vogelstein et al., 2009).

**2.4.1. A factorized approximation of the joint posteriors.** If the SNR in the calcium imaging is sufficiently high, then by definition the observed fluorescence data  $F_i$  will provide enough information to determine the underlying hidden variables  $X_i$ . Thus, in this case the joint posterior approximately factorizes into a product of marginals for each neuron  $i$ :

$$(13) \quad P[\mathbf{X}|\mathbf{F}; \theta] \approx \prod_{i \leq N} P[X_i|F_i; \tilde{\theta}_i].$$

We can take advantage of this because we have already estimated all the above marginals using the SMC method in Section 2.3. In particular, we can obtain the sufficient statistics  $P[n_i(t), \mathbf{h}_i(t)|\mathbf{F}; \tilde{\theta}_i]$  by forming a product over the marginals  $P[X_i(t)|F_i, \tilde{\theta}_i]$  obtained from Eq. (9). This factorized approximation entails a very significant gain in efficiency for two



reasons: first, it obviates the need to generate joint samples via the expensive blockwise-Gibbs approach described above; and second, because we can very easily parallelize the SMC step, inferring the marginals  $P[X_i(t)|F_i; \theta_i]$  and estimating the parameters  $\theta_i$  for each neuron on a separate processor. We will discuss the empirical accuracy of this approximation in more depth in the Results section.

**2.5. Estimating the functional connectivity matrix.** Computing the M-step for the connectivity matrix,  $\mathbf{w}$ , is an optimization problem with on the order of  $N^2$  variables. The auxiliary function Eq. (6) is concave in  $\mathbf{w}$ , and decomposes into  $N$  separable terms that may be optimized independently using standard ascent methods. To improve our estimates, we will incorporate two sources of strong *a priori* information via our prior  $P(\mathbf{w})$ : first, previous anatomical studies have established that connectivity in many neuroanatomical substrates is “sparse,” i.e., most neurons form synapses with only a fraction of their neighbors (Buhl et al., 1994; Thompson et al., 1988; Reyes et al., 1998; Feldmeyer et al., 1999; Gupta et al., 2000; Feldmeyer and Sakmann, 2000; Petersen and Sakmann, 2000; Binzegger et al., 2004; Song et al., 2005; Mishchenko et al., 2009), implying that many elements of the connectivity matrix  $\mathbf{w}$  are zero; see also (Paninski, 2004; Rigat et al., 2006; Pillow et al., 2008; Stevenson et al., 2008) for further discussion. Second, “Dale’s law” states that each of a neuron’s postsynaptic connections in adult cortex (and many other brain areas) must all be of the same sign (either excitatory or inhibitory). Both of these priors are easy to incorporate in the M-step optimization, as we discuss below.

**2.5.1. Imposing a sparse prior on the functional connectivity.** It is well-known that imposing sparseness via an  $L1$ -regularizer can dramatically reduce the amount of data necessary to accurately reconstruct sparse high-dimensional parameters (Tibshirani, 1996; Tipping, 2001; Donoho and Elad, 2003; Ng, 2004; Candes and Romberg, 2005; Mishchenko, 2009). We incorporate a prior of the form  $\ln p(\mathbf{w}) = \text{const.} - \lambda \sum_{i,j} |w_{ij}|$ , and additionally enforce the constraints  $|w_{ij}| < M$ , for a suitable constant  $M$  (since both excitatory and inhibitory cortical connections are known to be bounded in size). Since the penalty  $\ln p(\mathbf{w})$  is concave, and the constraints  $|w_{ij}| < M$  are convex, we may solve the resulting optimization problem in the M-step using standard convex optimization methods (Boyd and Vandenberghe, 2004). In addition, the problem retains its separable structure: the full optimization may be broken up into  $N$  smaller problems that may be solved independently.

**2.5.2. Imposing Dale’s law on the functional connectivity.** Enforcing Dale’s law requires us to solve a non-convex, non-separable problem: we need to optimize the concave function  $Q(\theta, \theta^{(l)}) + \ln P(\theta)$  under the non-convex, non-separable constraint that all of the elements in any column of the matrix  $\mathbf{w}$  are of a definite sign (either nonpositive or nonnegative). It is difficult to solve this nonconvex problem exactly, but we have found that simple greedy methods are quite efficient in finding good approximate solutions.

We begin with our original sparse solution, obtained as discussed in the previous subsection without enforcing Dale’s law. Then we assign each neuron as either excitatory or inhibitory, based on the weights we have inferred in the previous step: i.e., neurons  $i$  whose inferred postsynaptic connections  $w_{ij}$  are largely positive are tentatively labeled excitatory, and neurons with largely inhibitory inferred postsynaptic connections are labeled inhibitory. Neurons which are highly ambiguous may be unassigned in the early iterations, to avoid making mistakes from which it might be difficult to recover. Given the assignments  $a_i$  ( $a_i = 1$  for putative

---

**Algorithm 1** Pseudocode for estimating functional connectivity from calcium imaging data using EM;  $\eta^n$ ,  $\eta^F$ ,  $N_G$  are user-defined convergence tolerance parameters.

---

```

while  $|\mathbf{w}^{(l)} - \mathbf{w}^{(l-1)}| > \eta^w$  do
  for all  $i = 1 \dots N$  do
    while  $|\hat{\theta}_i^{(l)} - \hat{\theta}_i^{(l-1)}| > \eta^F$  do
      Approximate  $P[X_i(t)|F_i; \tilde{\theta}_i]$  using SMC (Section 2.3)
      Perform the M-step for the nuisance parameters  $\tilde{\theta}_i$  (Section 2.3)
    end while
  end for
  for all  $i = 1 \dots N$  do
    Approximate  $P[n_i(t), \mathbf{h}_i(t)|\mathbf{F}; \theta_i]$  using either the blockwise Gibbs
    method or the factorized approximation (Section 2.4)
  end for
  for all  $i = 1 \dots N$  do
    Perform the M-step on  $\theta_i$  using separable convex optimization methods (Section 2.5)
  end for
end while

```

---

excitatory cells,  $-1$  for inhibitory, and  $0$  for neurons which have not yet been assigned) we solve the convex, separable problem

$$(14) \quad \underset{a_i w_{ij} \geq 0, |w_{ij}| < M \quad \forall i,j}{\operatorname{argmax}} \quad Q(\theta, \theta^{(l)}) - \lambda \sum_{ij} |w_{ij}|$$

which may be handled using the standard convex methods discussed above. Given the new estimated connectivities  $\mathbf{w}$ , we can re-assign the labels  $a_i$ , or even flip some randomly to check for local optima. We have found this simple approach to be effective in practice.

*2.6. Specific implementation notes.* Pseudocode summarizing our approach is given in Algorithm 1. As discussed in Section 2.3, the nuisance parameters  $\tilde{\theta}_i$  may be initialized effectively using the methods described in (Vogelstein et al., 2009); then the full parameter  $\theta$  is estimated via EM, where we use the embedded-chain-within-blockwise-Gibbs approach discussed in Section 2.4 (or the cheaper factorized approximation described in Section 2.4.1) to obtain the sufficient statistics in the E step and the separable convex optimization methods discussed in Section 2.5 for the M step.

As emphasized above, the parallel nature of these EM steps is essential for making these computations tractable. We performed the bulk of our analysis on a 100-node cluster of Intel Xeon L5430 based computers (2.66 GHz). For 10 minutes of simulated fluorescence data, imaged at 30 Hz, calculations using the factorized approximation typically took 10-20 minutes per neuron (divided by the number of available processing nodes on the cluster), with time split approximately equally between (i) estimating the nuisance parameters  $\tilde{\theta}_i$ , (ii) approximating the posteriors using the independent SMC method, and (iii) estimating the functional connectivity matrix,  $\mathbf{w}$ . The hybrid embedded-chain-within-blockwise-Gibbs sampler was substantially slower, up to an hour per neuron per Gibbs pass, with the Gibbs sampler dominating the computation time, because we thinned the chain by a factor of five (since we found empirically that the autocorrelation of the Gibbs chain had a scale of about five time steps).

*2.7. Simulating a neural population.* To test the described method for inferring functional connectivity from calcium imaging data, we simulated networks (according to our model,

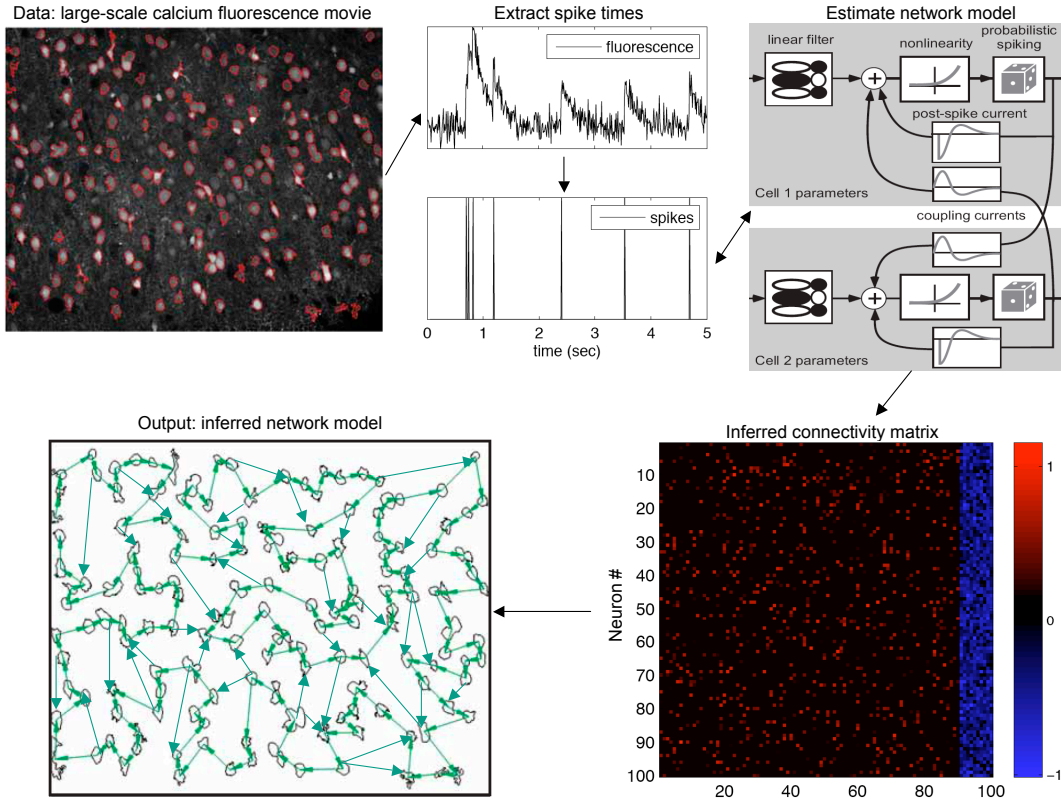


FIG 3. *Schematic overview. The raw observed data is a large-scale calcium fluorescence movie, which is pre-processed to correct for movement artifacts (in the in vivo setting) and find regions-of-interest (i.e., putative neurons); note that we have omitted details of these important preprocessing steps in this paper. Given the fluorescence traces from each neuron, we estimate the underlying spike trains (i.e., in time series of neural activity) using statistical deconvolution methods. Then we estimate the parameters of a network model, given the observed data. Our major goal is to obtain an accurate estimate of the network connectivity matrix, which summarizes the information we are able to infer about the local neuronal microcircuit. This figure adapted from personal communications with R. Yuste, B. Watson, and A. Packer.*

Eqs. (1) – (5)) of spontaneously firing randomly connected neurons. Although simulations ran at 1 msec time discretization, imaging rate was assumed to be much slower. Simulations lasted anywhere between 5 minutes and 1 hours (of simulated time). Model parameters were chosen based on experimental data available in the literature for cortical neural networks (Braitenberg and Schuz, 1998; Gomez-Urquijo et al., 2000; Lefort et al., 2009; Sayer et al., 1990).

More specifically, the network contained 80% of excitatory and 20% inhibitory neurons (Braitenberg and Schuz, 1998; Gomez-Urquijo et al., 2000), each respecting Dale’s law. Neurons were randomly connected to each other with probability 0.1 (Braitenberg and Schuz, 1998; Lefort et al., 2009). Synaptic weights for excitatory connections, as defined by EPSP peak amplitude, were randomly drawn from exponential distribution with the mean of  $0.5\mu V$  (Lefort et al., 2009; Sayer et al., 1990). Inhibitory connections were also drawn from exponen-

tial distribution; their strengths chosen so as to balance excitatory and inhibitory currents in the network, and achieve an average firing rate of  $\approx 5$  Hz (?). Practically, this meant that the mean strength of inhibitory connections was about 10 times larger than that of the excitatory connections.

Note that EPSP peak amplitudes cannot be used directly in Eq. (1). A Synaptic weight in our model —  $w_{ij}$  in Eq. (1) — is a dimensionless quantity representing the change in the spiking probability of neuron  $i$  given neuron  $j$  fired; whereas EPSP peak amplitude describes physiologically measured change in the membrane voltage of a neuron due to synaptic currents triggered by spike in neuron  $j$ . We must therefore find a way to relate the two.

Consider the above model for spiking, Eqs. (1) – (3). Let  $\delta P$  be the difference between the probability of neuron  $i$  spiking given that neuron  $j$  spiked in the previous time bin,  $P[n_i(t) = 1|n_j(t - \Delta) = 1]$ , and the probability of neuron  $i$  spiking given that neuron  $j$  did *not* spike in the previous time bin,  $P[n_i(t)|n_j(t - \Delta) = 0]$ :

$$\begin{aligned} \delta P &= P[n_i(t) = 1|n_j(t - \Delta) = 1] - P[n_i(t) = 1|n_j(t - \Delta) = 0] \\ (15) \quad &= \exp[-e^{b_i + w_{ij}} \Delta \tau^h] - \exp[-e^{b_i} \Delta \tau^h] \end{aligned}$$

Now consider a simple, stochastic, integrate-and-fire neuron, with baseline voltage zero, spiking threshold one, EPSP amplitude  $V_E$ , and variance  $\sigma_v^2$ :

$$\begin{aligned} V_i(t) &= V_i(t - \Delta) + V_E \delta(n_j(t - \Delta)) + \sigma_v \sqrt{\Delta} \varepsilon_i(t), & \text{if } V_i(t) < 1 \\ (16) \quad V_i(t) &= 0 & \text{if } V_i(t) \geq 1 \end{aligned}$$

In such a model, we again write  $\delta P$ :

$$\begin{aligned} \delta P &= \int_1^\infty \mathcal{N}(V_i(t - \Delta), \sigma^2) dV_i(t - \Delta) - \int_1^\infty \mathcal{N}(V_i(t - \Delta) + V_E, \sigma^2) dV_i(t - \Delta) \\ (17) \quad &= g(V_E) \end{aligned}$$

A little algebra yields:

$$(18) \quad w_{ij} = \ln \left[ -\frac{1}{\Delta \tau^h} \ln \left[ g(V_E) + \exp \left( -e^{b_i} \Delta \tau^h \right) \right] \right] - b_i$$

which we evaluated explicitly using parameters in accordance with the literature.

PSP shapes were modeled as an alpha function (Koch, 1999), by differencing two exponentials, corresponding to a sharp rise and relatively slow decay (Sayer et al., 1990). We neglected conduction delays, given that the time delay below  $\sim 1$  msec expected in local cortical circuit was smaller than the time step of our computer simulation. Each neuron also had an exponential refractory current (Koch, 1999).

Parameters for the internal calcium dynamics and fluorescence observations were chosen according to our experience with several cells analyzed using algorithm of (Vogelstein et al., 2009), and conformed to previously published results (Yuste et al., 2006; Helmchen et al., 1996; Brenowitz and Regehr, 2007). Table 2 summarizes the details for each of the parameters in our model.

### 3. Results.

3.1. *Simulating neural activity in a neural population.* To test the described method for inferring functional connectivity from calcium imaging data, we simulated networks (according to our model, Eqs. 1 – 5) of spontaneously firing randomly connected neurons. Although simulations ran at 1 msec time discretization, imaging rate was assumed to be much slower. Simulations lasted anywhere between 5 minutes and 1 hours (of simulated time). Model parameters were chosen based on experimental data available in the literature for cortical neural networks (Braitenberg and Schuz, 1998; Gomez-Urquijo et al., 2000; Lefort et al., 2009; Sayer et al., 1990).

More specifically, the network contained 80% of excitatory and 20% inhibitory neurons (Braitenberg and Schuz, 1998; Gomez-Urquijo et al., 2000), each respecting Dale’s law. Neurons were randomly connected to each other with probability 0.1 (Braitenberg and Schuz, 1998; Lefort et al., 2009). Synaptic weights for excitatory connections, as defined by EPSP peak amplitude, were randomly drawn from exponential distribution with the mean of  $0.5\mu V$  (Lefort et al., 2009; Sayer et al., 1990). Inhibitory connections were also drawn from exponential distribution; their strengths chosen so as to balance excitatory and inhibitory currents in the network, and achieve an average firing rate of  $\approx 5$  Hz (?). Practically, this meant that the mean strength of inhibitory connections was about 10 times larger than that of the excitatory connections.

Note that EPSP peak amplitudes cannot be used directly in Eq. 1. Really,  $w_{ij}$  in Eq. 1 is a dimensionless quantity representing the change in the spiking probability of neuron  $i$  given neuron  $j$  fired, while EPSP peak amplitude describes physiologically measured change in the membrane voltage of a neuron due to synaptic currents triggered by spike in neuron  $j$ . These two quantities, therefore, are dramatically different and we need to find a way to relate the two.

For that, we first point out that in order to trigger an immediate spike in a neuron that typically has its membrane voltage  $V_b$   $\mu V$  below the spiking threshold  $n_E = V_b/V_E$  simultaneous EPSPs with the peak amplitude  $V_E$  would be necessary. Therefore, we propose that the change in the spiking probability of a neuron due to excitatory synaptic current  $V_E$  can

TABLE 1

*Table of simulation parameters.  $\mathcal{E}(\lambda)$  indicates an exponential distribution with mean  $\lambda$ , and  $\mathcal{N}_p(\mu, \sigma^2)$  indicates a normal distribution with mean  $\mu$  and variance  $\sigma^2$ , truncated at lower bound  $p\mu$ . Units (when applicable) are given with respect to mean values (i.e., units are squared for variance).*

Total neurons	10-500	
Excitatory neurons	80%	
Connections sparseness	10%	
Baseline firing rate	5	Hz
EPSP peak height	$\sim \mathcal{E}(0.5)$	$\mu V$
IPSP peak height	$\sim -\mathcal{E}(2.3)$	$\mu V$
EPSP rise time	1	msec
IPSP rise time	1	msec
EPSP decay time	$\sim \mathcal{N}_{0.5}(10, 2.5)$	msec
IPSP decay time	$\sim \mathcal{N}_{0.5}(20, 5)$	msec
refractory time	$\sim \mathcal{N}_{0.5}(10, 2.5)$	msec
Calcium std. $\sigma_c$	$\sim \mathcal{N}_{0.4}(28, 10)$	$\mu M$
Calcium jump after spike, $A_c$	$\sim \mathcal{N}_{0.4}(80, 20)$	$\mu M$
Calcium baseline, $C_b$	$\sim \mathcal{N}_{0.4}(24, 8)$	$\mu M$
Calcium decay time, $\tau_c$	$\sim \mathcal{N}_{0.4}(200, 60)$	msec
Mean photon budget $\alpha_c$	1-80	Kph/neuron/frame
Dissociation constant, $K_d$	200	$\mu M$

be approximately defined as (so that  $\delta P_E n_E \approx 1$ )

$$(19) \quad \delta P_E = V_E/V_b.$$

At the same time, according to Eq. 1, the same change in the spiking probability of a neuron  $i$  following the spike of a neuron  $j$  should be defined in GLM as

$$(20) \quad \delta P_E = \exp[-e^{b_i+w_{ij}}\tau_w] - \exp[-e^{b_i}\tau_w]$$

Here  $\tau_w$  is the typical EPSP time-scale, i.e. the time over which EPSP of one neuron,  $j$ , significantly affects the firing probability of the other neuron,  $i$ .

Equating Eq. 19 and Eq. 20, we arrive at the proposition for our link function for physiologically measured EPSP peak amplitude,  $V_E$ , and GLM weight,  $w_{ij}$ :

$$(21) \quad w_{ij} = \ln(-\ln(e^{-r_i\tau_w} - V_E/V_b)/r_i\tau_w).$$

Here  $r_i = \exp(b_i)$  is the base firing rate of neuron  $i$ . PSP shapes were modeled as an alpha function (Koch, 1999), by differencing of two exponentials, corresponding to a sharp rise and relatively slow decay (Sayer et al., 1990). We neglected conduction delays, given that the time delay below  $\sim 1$  msec expected in local cortical circuit was smaller than the time step of our computer simulation. Each neuron also had an exponential refractory current (Koch, 1999).

Parameters for the internal calcium dynamics and fluorescence observations were chosen according to our experience with several cells analyzed using algorithm of (Vogelstein et al., 2009), and conformed to other experimental observations (Yuste et al., 2006; Helmchen et al., 1996; Brenowitz and Regehr, 2007). Each parameter was generated from a normal distribution with specified mean and variance at about 30% of the mean, truncated at the lower bound at about 30% of the mean value. Table 2 summarizes the details for each of the parameters in our model.

TABLE 2

Table of simulation parameters.  $\mathcal{E}(\lambda)$  indicates an exponential distribution with mean  $\lambda$ , and  $\mathcal{N}_p(\mu, \sigma^2)$  indicates a normal distribution with mean  $\mu$  and variance  $\sigma^2$ , truncated at lower bound  $p\mu$ .

Total neurons	10-500
Excitatory neurons	80%
Connections sparseness	10%
Baseline firing rate	5 Hz
EPSP peak height	$\sim \mathcal{E}[0.5\mu V]$
IPSP peak height	$\sim \mathcal{E}[2.3\mu V]$
EPSP rise time	1 msec
IPSP rise time	1 msec
EPSP decay time	$\sim \mathcal{N}_{0.5}[10 \text{ msec}, (2.5 \text{ msec})^2]$
IPSP decay time	$\sim \mathcal{N}_{0.5}[20 \text{ msec}, (5 \text{ msec})^2]$
refractory time	$\sim \mathcal{N}_{0.5}[10 \text{ msec}, (2.5 \text{ msec})^2]$
Calcium std. $\sigma_c$	$\sim \mathcal{N}_{0.4}[28\mu M, (10\mu M)^2]$
Calcium jump after spike, $A_c$	$\sim \mathcal{N}_{0.4}[80\mu M, (20\mu M)^2]$
Calcium baseline, $C_b$	$\sim \mathcal{N}_{0.4}[24\mu M, (8\mu M)^2]$
Calcium decay time, $\tau_c$	$\sim \mathcal{N}_{0.4}[200 \text{ msec}, (60 \text{ msec})^2]$
Mean photon budget $\alpha_c$	1–80 Kph/neuron/frame
Dissociation constant, $K_d$	200 $\mu M$

**3.2. Inferring functional connectivity from the simulated calcium imaging data.** With neural population activity prepared as described in the previous section, we used our inference algorithms to reconstruct the functional connectivity matrix from simulated fluorescence data. Specifically, we estimated the connectivity matrix using both the embedded-chain-within-blockwise-Gibbs approach as well as factorized approximation, Figure 4. We found that factorized approximation was able to provide reconstructions almost as accurate as the exact embedded-chain-within-blockwise-Gibbs approach —  $r^2 = 0.47$  versus  $r^2 = 0.48$  — when parameters corresponded to a realistic preparation, given 10 minutes of simulation data, and a population of  $N = 25$  neurons. We furthermore estimated the weights using GLM from the true spike trains, and the true spike trains down-sampled to the frame rates of calcium imaging,  $r^2 = 0.7$  and  $r^2 = 0.57$  respectively. thus, the quality of our estimates using the fluorescence traces was worse than those obtained from the the true down-sampled spike trains although for SNR of fluorescence data the  $r^2$  values for obtained reconstructions approached that of down-sampled true spike trains, Figure 9. Example of what we understand by high SNR (can be used for functional connectivity inference) and low SNR (cannot be used for functional connectivity inference) are shown in Figure 9 on two fluorescence traces from real in-vivo data.

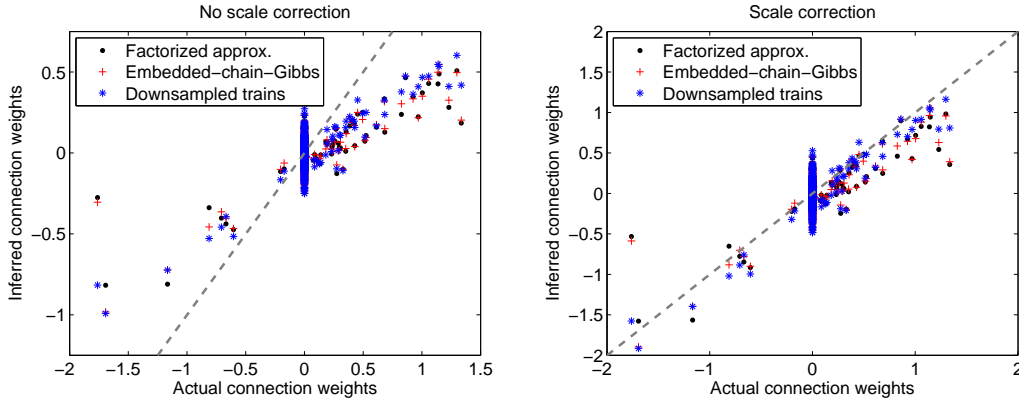


FIG 4. Functional connectivity matrix can be reconstructed from calcium imaging data. Inferred connection weights are shown in a scatter plot versus real connection weights, with inference performed using factorized approximation, exact embedded-chain-within-blockwise-Gibbs approach, and true spike trains observed at the frame rate of the calcium imaging. Network of  $N = 25$  neurons was used, firing at  $\approx 5$  Hz, and imaged for  $T=600$  sec at intermediate SNR (photon budget 10Kph/neuron/frame, see below).  $r^2 = 0.47$  for factorized approximation,  $r^2 = 0.48$  for embedded-chain-within-blockwise-Gibbs, and  $r^2 = 0.57$  for true down-sampled spike trains. Factorized approximation produced results almost as accurate as the exact embedded-chain-within-blockwise-Gibbs approach, and almost as accurate as the original spikes. Inferred connectivity weights were always scaled with respect to true connectivity due to time discretization bias (see main text). This bias can be successfully calculated theoretically and removed from the estimate of  $\mathbf{w}$ .

**3.3. Impact of coarse time discretization of calcium imaging data and scale bias in inferred connection weights.** Spike trains, necessary to evaluate functional connectivity matrix  $\mathbf{w}$ , here were inferred with discretization into time-bins corresponding to the frame-rate of calcium imaging fluorescence data. In principle, one could use super-resolution feature of (Vogelstein et al., 2009) to obtain spike trains with arbitrarily small time step  $\Delta \rightarrow 0$ . However, the problem in that case is that the spikes, inferred from fluorescence data, contain inaccuracy in their temporal position  $\approx 1/\text{frame-rate}$ , due to the time-discretization of the

underlying fluorescence trace. Thus, when we super-resolve spikes using (Vogelstein et al., 2009), the spike pairs such that a spike of neuron  $i$  closely follows a spike of neuron  $j$  can be often confused with such where a spike of neuron  $j$  closely follows a spike of neuron  $i$ . It, therefore, becomes impossible to determine which neuron fired first, and which neuron was pre-synaptic or post-synaptic in given pair of neurons  $i, j$ . More specifically, when using  $\Delta \rightarrow 0$ , we observed large errors in  $\mathbf{w}$ ,  $\text{var}[\mathbf{w}] \propto \mathbf{w} + \mathbf{w}^T$  - because of inaccuracies in temporal position of spikes inferred from calcium imaging it became impossible to reliably distinguish which neuron causally preceded which other neuron, and only a-causal connectivity matrix  $(\mathbf{w} + \mathbf{w}^T)/2$  could be determined.

To circumvent this problem, we (down-)sampled the time-axis in bins of size  $\Delta = 1/\text{frame-rate}$ , and treated all spike pairs that occurred within the same time-bin as coincidental. This successfully counteracted the above problem and, additionally, allowed to perform calculations substantially faster by using larger  $\Delta$ . At the same time, this resulted in scale bias that all our inferred connectivity matrices consistently exhibited, Figure 4. This bias may be successfully understood and corrected from the following time-discretization argument. Specifically, estimating the magnitude of the connection weight  $w_{ij}$  is based on empirically evaluating the spike-triggered probability of neuron  $i$  to fire, conditioned on neuron  $j$ . Most significant change in the spiking probability of neuron  $i$ , conditioned on neuron  $j$ , occurs within  $\tau_w \approx 10 - 20$  msec from a spike of neuron  $j$ . When spike trains are down-sampled into large time-bins, e.g.  $\Delta = 30$  msec, a significant fraction of close spike pairs appears coincidental and not causal, as both spikes from neuron  $i$  and neuron  $j$  within  $\approx \tau_w$  from each other are often assigned to the same time-bin. As we discussed in the previous paragraphs, such close spike pairs typically introduce a great deal of noise in the estimate of  $\mathbf{w}$ . When  $\Delta$  is large, however, most of such unreliable spike pairs would be considered coincidental and would not affect  $\mathbf{w}$  estimate. At the same time, all of such close pairs would be lost if we were to empirically evaluate the spike-triggered probabilities, which would have led us to believe in a lower than the actual  $w_{ij}$ .

To estimate the magnitude of this time-discretization bias quantitatively, we consider a significantly simplified case of two neurons coupled with a small weight  $w_{12}$ , and firing with baseline firing rate of  $r = f(b) = \exp(b)$ ,  $b \gg w_{12}$ . A sufficient statistics for estimating  $w_{12}$  in this case is, e.g.:

$$\begin{aligned}
 (22) \quad S &= E \left[ \int_{t'}^{t'+T} dt n_1(t) | n_2(t') = \text{spike}, n_2(t) = \text{no spike } \forall t' < t < t' + T \right] \\
 &\approx rT + f'(b) \int_{t'}^{t'+T} dt w_{12} \exp(-t/\tau_w) \\
 &\approx rT + f'(b) w_{12} \tau_w,
 \end{aligned}$$

where  $\tau_w \ll T \ll 1/r$ , and

$$(23) \quad w_{12} = (S - rT) / f'(b) \tau_w.$$

Now, if the spike trains were down-sampled into time-bins of size  $\Delta$ , we estimate statistics  $S$  with a discrete sum:

$$\begin{aligned}
 (24) \quad S^{ds} &= E \left[ \sum_{t=t'+\Delta}^{t'+\Delta+T} n_1^{ds}(t) | n_2^{ds}(t') = 1, n_2^{ds}(t) = 0 \forall t' < t < t' + T \right] \\
 &\approx rT + f'(b) \int_0^{\Delta} \frac{dt'}{\Delta} \int_{\Delta}^{\Delta+T} dt w_{12} \exp(-(t-t')/\tau_w) \\
 &\approx rT + f'(b) w_{12} \frac{1 - \exp(-\Delta/\tau_w)}{\Delta/\tau_w^2}.
 \end{aligned}$$



$n^{ds}(t)$  here are down-sampled spikes, i.e. the spikes defined on a grid  $t = 0, \Delta, 2\Delta, \dots$ . In the second equality we took into account that the true position of the spike of the second neuron,  $n_2^{ds}(t')$ , may be uniformly distributed in first time-bin, here  $[0, \Delta]$ , and discrete sum over  $t$  is from second time-bin  $[\Delta, 2\Delta]$  to  $[\mathcal{T}, \mathcal{T} + \Delta]$ , i.e. over all spikes of the first neuron that occurred in any of the strictly subsequent time-bins up to  $\mathcal{T} + \Delta$ . If we were to naively apply GLM Eq. 23 here using down-sampled estimate  $S^{ds}$ , we would have obtained

$$(25) \quad w_{12}^{ds} \approx \frac{1 - \exp(-\Delta/\tau_w)}{\Delta/\tau_w} w_{12}.$$

This is the scale bias that we observe. In Figure 5 we plot the scale bias from Eq. 25 versus that empirically deduced from our simulations for different values of  $\Delta$ . As can be seen in Figure 5, Eq. 25 describes observed scale bias very well.

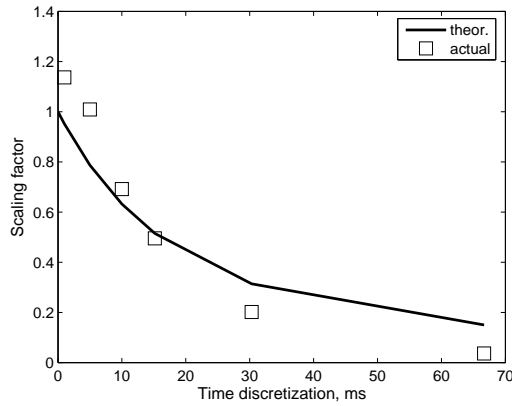


FIG 5. The low-frame rate of calcium imaging can explain the scale bias in inferred connectivity weights in Figure 4. Theoretically, scale bias may be evaluated by calculating what fraction of spikes from two neurons would occur within a single time-bin of width  $\Delta$  (c.f. Eq. 25). Plotted such theoretically calculated scale bias (line) vs. that observed empirically from our simulations (box), from a simulation of  $N = 25$  neurons,  $T = 10$  min. The error-bars correspond to 95% confidence intervals for scale bias estimate.

**3.4. Impact of using priors on the inference.** Taking into account simple prior information about the connectivity matrix results in dramatic improvement of the inferred connectivity matrix, Figure 6 and 7, allowing successful reconstruction from as little as 5 min of calcium imaging data, and for  $T \approx 10$  min achieving the same level of accuracy otherwise requiring up to  $T \approx 1$  hour of calcium imaging, Figure 10. For example, in a network of  $N = 50$  neurons imaged for  $T = 10$  min,  $r^2$  is increased from  $r^2 = 0.64$  to  $r^2 = 0.85$  when sparse prior was enforced. Furthermore,  $\mathbf{w}$  estimates calculated with sparse prior allow reliable determination which neurons are connected, or which neurons are inhibitory or excitatory in nature, Figure 7. At the same time, sparse prior introduces additional scale bias into connectivity estimates, which, therefore, effectively destroys information about the true scale of the connection weights. Dale's prior, on the other hand, only leads to 10% in the correlation coefficient  $r^2$  of the reconstructed connectivity matrix, and was not found significant. In case when sparse prior was initially enforced, enforcing Dale's prior typically resulted in no improvement to  $\mathbf{w}$  at all.

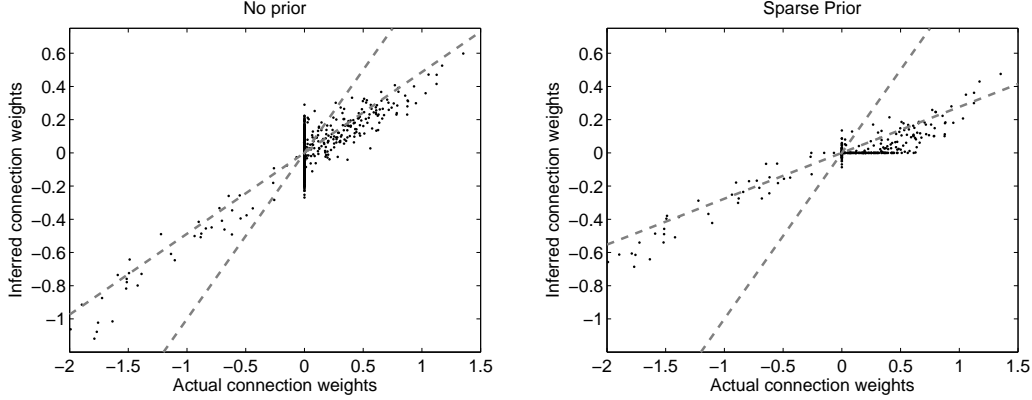


FIG 6. Incorporating simple priors on the distribution of connectivity weights, such as exponential sparseness prior, is essential to achieve much more accurate reconstructions from a smaller amount of calcium imaging data. Shown here are the connection weights reconstructed using GLM (left panel) or sparse-prior GLM (right panel) are shown in a scatter plot for a network of  $N = 50$  neurons, firing at  $\approx 5$  Hz, and imaged for  $T = 600$  sec.  $r^2 = 0.64$  for simple GLM and  $r^2 = 0.85$  for sparse-GLM. Since original  $\mathbf{w}$  is sparse, noise in the estimates of  $w_{ij} = 0$  results in a vertical line at zero in the left panel. Likewise, sparse prior results in many small  $w_{ij}$  to be deduced as zeros, which produces the horizontal line at zero in the right panel.

**3.5. Impact of different imaging frame rates, noise levels, and durations on the estimator accuracy.** What minimal conditions for the experimental setup should be met to allow successful reconstruction of the connectivity from calcium imaging data? In Figures 8 – 10 we address this question. Figure 8 shows the quality of the inferred connectivity matrix as function of the imaging frame rate - imaging frame rates 30-60 Hz are needed to achieve meaningful reconstruction results. Frame rates  $\approx 100$  Hz allow achieving the same level of the connectivity matrix reconstruction that is possible with the exact knowledge of the true spike trains. Imaging frame 30-60 Hz are already possible in existing experimental setups, and imaging at 100 Hz may be technologically possible in the future (Nguyen et al., 2001; Reddy and Saggau, 2005; Iyer et al., 2006; Salome et al., 2006; Reddy et al., 2008)

Figure 9 shows the quality of the inferred connectivity matrix as function of effective SNR and photon budget. Operationally, we define effective SNR as

$$(26) \quad eSNR = \frac{E[F_i(t) - F_i(t-1)|n_i(t) = 1]}{E[(F_i(t) - F_i(t-1))^2/2|n_i(t) = 0]^{1/2}},$$

and photon budget as  $\gamma^{-1}$ . Photon budget corresponds to the number of photons collected from single neuron within a single frame, at the peak of fluorescence intensity. From our experience with the analysis of real cells (Vogelstein et al., 2009), the eSNR in real data was  $\sim 3$  for in vivo data collected at 15 Hz and  $\sim 9$  for in vitro data at the same frame rate. As can be seen from Figure 9, the effective SNR necessary for accurate reconstructions was  $\approx 5$ . This eSNR corresponded to photon budgets of  $\approx 10$  Kph/neuron/frame. For lower eSNR, the amount of noise in calcium imaging data degraded inferred connectivity matrices significantly.

Finally, Figure 10 shows the quality of the inferred connectivity matrix as function of the experiment duration. The minimal amount of data for a particular  $r^2$  depended substantially on whether priors were enforced in M-step. In particular, for the M-step lacking a sparse prior, the calcium imaging duration necessary to achieve  $r^2 = 0.5$  for the reconstructed connectivity matrix was  $T \approx 10$  min, and  $r^2 = 0.75$  was achieved at  $T \approx 30$  min. When M-step enforced sparseness prior,  $r^2 > 0.7$  was achieved already at  $T \sim 5$  min. Furthermore, we observed

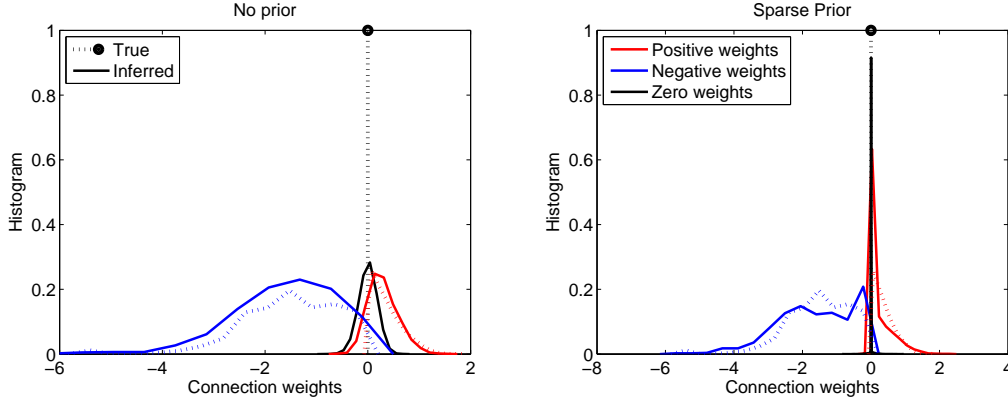


FIG 7. The distribution of inferred connection weights using GLM (left) and sparse GLM (right) vs. true distributions. When sparse exponential prior is enforced, dispersion in inferred connection weights is substantially reduced and, in particular, it becomes possible to reliably determine which neural pairs are connected, and which neurons are excitatory or inhibitory. Distributions are shown for a network of  $N = 200$  neurons, firing at  $\approx 5$  Hz, and imaged for  $T = 600$  sec.

that the accuracy of the reconstruction did not deteriorate with the size of the imaged neural population, whereas the same reconstruction quality was observed with the same amount of data for  $N = 50 - 200$  neurons. This, at first unexpected, result is the direct consequence of the structure of the covariance matrix for  $\mathbf{w}$ , as will be discussed below. In all cases, good reconstructions were possible to obtain with only  $T \sim 5-30$  min of calcium imaging data.

**3.6. Accuracy of the estimates and Fisher information matrix.** Here we calculate theoretically the amount of spike trains data necessary to accurately estimate the functional connectivity matrix  $\mathbf{w}$ . For clarity, we assume here that  $\Delta \rightarrow 0$ , and so  $f(J) \approx e^J \Delta$ , and that the spike trains are known perfectly, i.e. there is no corruption due to inference from low-SNR calcium imaging data. As we shown above, for sufficient SNR this latter condition can be certainly achieved by calcium imaging data. We also assume that the spikes only couple over a single time bin, i.e.  $h_{ij}(t) \equiv n_j(t - \Delta)$ . Then, using GLM likelihood

$$\begin{aligned}
 -\ln P[\mathbf{w}|\mathbf{X}] &\sim -\ln P[\mathbf{X}|\mathbf{w}] = \sum_{i,t} [n_i(t) \ln f(J_i(t)) + (1 - n_i(t))(1 - f(J_i(t)))], \\
 J_i(t) &= b_i(t) + \sum_j w_{ij} h_{ij}(t), \\
 h_{ij}(t) &= n_j(t - \Delta),
 \end{aligned}
 \tag{27}$$

the Fisher information matrix for  $P[\mathbf{w}|\mathbf{X}]$  is:

$$\begin{aligned}
 C_{ij;i'j'}^{-1} &= \left[ \frac{\partial(-\ln P[\mathbf{w}|\mathbf{X}])}{\partial w_{ij} \partial w_{i'j'}} \right] = - \delta_{ii'} \sum_t \left[ n_i(t) n_j(t - \Delta) n_{j'}(t - \Delta) \left( -\frac{f'(J_i(t))^2}{f(J_i(t))^2} + \frac{f''(J_i(t))}{f(J_i(t))} \right) - \right. \\
 &\quad \left. - (1 - n_i(t)) n_j(t - \Delta) n_{j'}(t - \Delta) f''(J_i(t)) \right].
 \end{aligned}
 \tag{28}$$

where  $f'$  and  $f''$  correspond to the first and the second derivatives of our linking function (c.f Eq. 1), and  $\delta_{ii'}$  is the Kronecker's delta symbol,  $\delta_{ii'} = 1$  for  $i = i'$ , and  $\delta_{ii'} = 0$  otherwise. Letting  $f(J) = e^J \Delta$ , the first term in the sum in Eq. 28 cancels out, and the rest may be

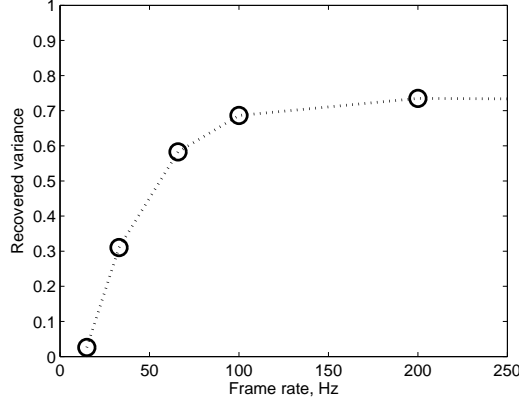


FIG 8. Accuracy of the inferred connectivity as function of the frame rate of calcium imaging. Connectivity matrix here was inferred from the original spike trains observed at corresponding frame rates, thus establishing the upper performance bound on the inference from calcium imaging data. A network of  $N = 25$  neurons, firing at  $\approx 5$  Hz and imaged for  $T = 600$  sec was to generate this plot.

rewritten as:

$$\begin{aligned}
 C_{ij;i'j'}^{-1} &= \delta_{ii'} TP[n_i(t) = 0, n_j(t - \Delta) = 1, n_{j'}(t - \Delta) = 1] \times \\
 (29) \quad &\times E[e^{J_i(t)} | n_i(t) = 0, n_j(t - \Delta) = 1, n_{j'}(t - \Delta) = 1] \\
 &= \delta_{ii'} T [(r\tau_w)\delta_{jj'} + O((r\tau_w)^2)] r.
 \end{aligned}$$

Here,  $TP[n_i(t) = 0, n_j(t - \Delta) = 1, n_{j'}(t - \Delta) = 1]$  describes the number of nonzero terms in Eq. 28, corresponding to the condition that  $(1 - n_i(t))n_j(t - \Delta)n_{j'}(t - \Delta)$  is only nonzero when  $n_i(t) = 0, n_j(t - \Delta) = 1, n_{j'}(t - \Delta) = 1$ .  $r = E[e^{J_i(t)} | n_i(t) = 0, n_j(t - \Delta) = 1, n_{j'}(t - \Delta) = 1]$ , then, corresponds to the average value of  $f''(J_i(t))$ , conditional on such nonzero events.  $r\tau_w \ll 1$  is the probability for a neuron to spike over the time-interval  $\tau_w$ .

The Fisher information matrix is block-diagonal,  $C_{ij;i'j'}^{-1} \propto \delta_{ii'}$ , due to the structure of the log-likelihood  $P[\mathbf{X}|\mathbf{w}]$ , in particular, that it is represented as a sum over  $i$  of independent terms, Eq. 27. But also from Eq. (29) we observe that Fisher information matrix is predominantly diagonal,  $C_{ij;i'j'}^{-1} \propto \delta_{ii'}\delta_{jj'}$ , and thus the covariance matrix  $C$  can be computed trivially:

$$(30) \quad C = (rT)^{-1}(r\tau_w I + O((r\tau_w)^2))^{-1} = (r^2\tau_w T)^{-1}I + O((r\tau_w)^2)$$

For successful determination of the functional connectivity matrix  $\mathbf{w}$ , the variance  $C$  should be made smaller than the typical scale  $\langle \mathbf{w}^2 \rangle$ , thus:

$$(31) \quad T \sim (\langle \mathbf{w}^2 \rangle r^2 \tau_w)^{-1}.$$

For typical values of  $\mathbf{w}^2 \approx 0.1$ ,  $r \approx 5$  Hz and  $\tau_w \approx 10$  msec, with this order of magnitude estimate we obtain  $T$  of the order of hundred seconds. This theoretical estimate of the necessary amount of fluorescent data is in good agreement with our simulations.

Finally, because  $C^{-1}$  is diagonal, this scale of  $C$  does not depend on the number of neurons in the imaged neural population,  $N$ . Thus, the variance of the estimate  $\mathbf{w}$  does not degrade with the size of the imaged population,  $N$ , for the same amount of data,  $T$ .

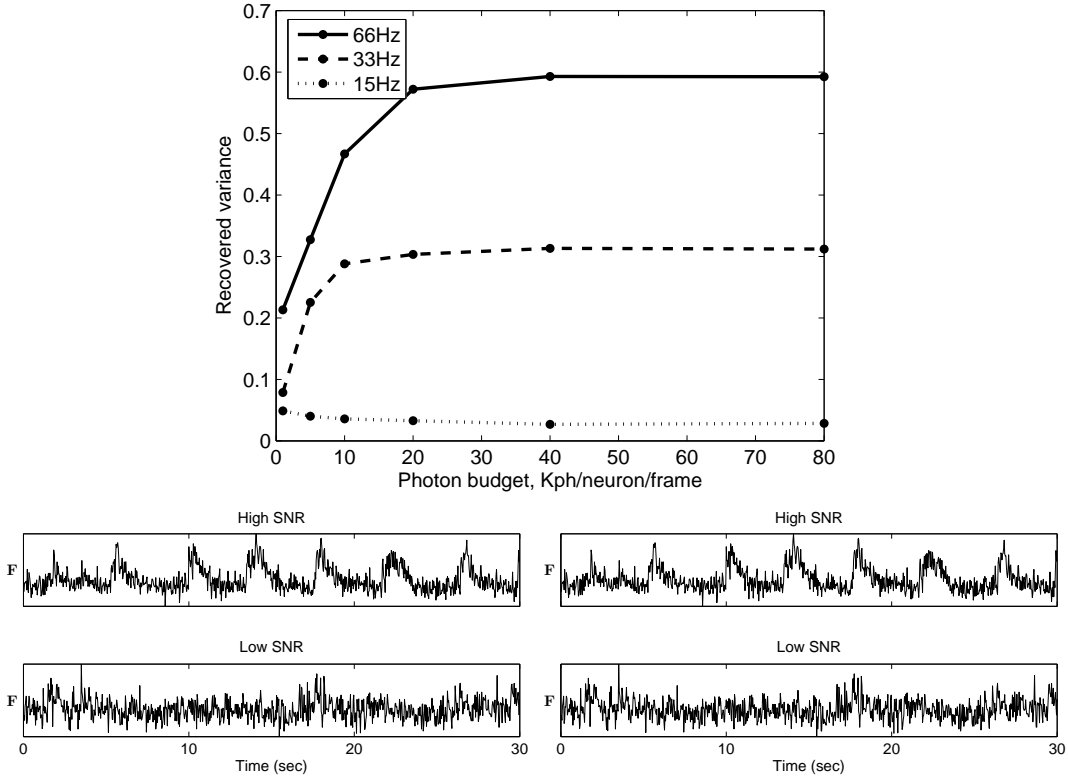


FIG 9. Accuracy of inferred connectivity as function of the noise amount in the calcium imaging data, as quantified by photon budget, per neuron-frame, for frame rates of 15 Hz, 33 Hz and 66 Hz. Photon counts on the order of 10-20 Kph/frame/neuron are required to achieve the upper bound due by the frame rate. Connectivity matrix here was inferred from simulated fluorescence data using factorized approximation algorithm. Simulation conditions are the same as in Figure 8. Vertical black lines correspond to the two example traces in the lower panels, left to right respectively.

3.7. *Impact of strong correlations and deviations from generative model on the inference.* “Anatomical” connectivity was recovered in our experiments despite potential problems noted in the literature [XXX], e.g. such as common input from correlated neurons. This is primarily due to the particular form of the activity in our neural networks, whereas firing of neurons occurred independently, thus, allowing GLM explore the full range of possible input configurations and disentangle common inputs.

Estimation of the functional connectivity is fundamentally routed in observing changes in the spike rate conditioned on the state of the other neurons. Intuitively, such estimation can be compared to observing changes in  $f(\mathbf{n}(t)) \propto \exp(\sum_j w_{ij} n_j(t))$  for different neural configurations  $\mathbf{n}(t)$ , i.e. estimating a vector  $\mathbf{w}_i$  from a number of dot-products  $\mathbf{w}_i \cdot \mathbf{n}(t)$ . In order to properly estimate all components of  $\mathbf{w}_i$  the set of available  $\mathbf{n}(t)$  should be rich enough to span all  $N$  dimensions of  $\mathbf{w}_i$ . In case of independent firing such condition is clearly satisfied. Should this condition be violated, however, e.g. due to high correlation between spiking of few neurons, spike trains may not provide access to the true vector  $\mathbf{w}_i$ , and the connection weights inferred from such activity data may effectively “aggregate” true connection weights in arbitrary linear combinations.

We carried out a simulation of hypothetical “strongly” coupled neural network, where

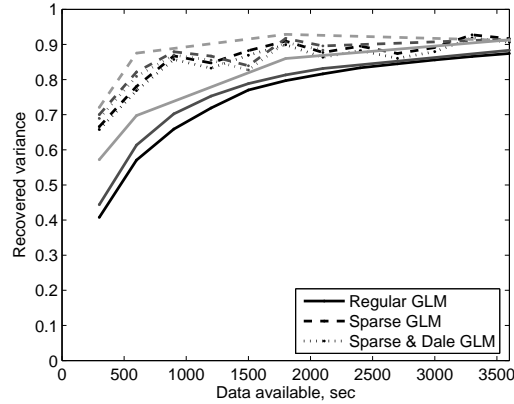


FIG 10. Accuracy of inferred connectivity as function of the imaging time and neural population size. Incorporating simple priors such as exponential sparseness prior allows to boost dramatically the reconstruction’s quality (dashed lines). In this latter case,  $T = 300$  sec is already sufficient to recover 70% of the variance in the connection weights. Incorporating Dale’s prior leads to only marginal improvement (dotted line). As shown in the methods, reconstruction accuracy does not depend on the neural population size  $N$ . Here, neural population from  $N = 10$  to  $N = 200$  were simulated for different  $T$ , where  $N = 200$  (gray) and  $N = 100$  (black) are shown. All networks were prepared in similar state by adjusting strength of inhibitory connections to achieve similar mean firing rate  $\approx 5$  Hz, although actual firing rate could vary.

in addition to weak sparse connectivity we introduced sparse random strong connectivity component. In a sense, we allowed a fraction of neurons to couple strongly to the other neurons, thus, making them “command” neurons “driving” the activity of the rest of the population. The strength of strong connectivity component was chosen to dynamically build up the actual firing rate from the baseline rate of  $r = \exp(b) \approx 1$  Hz to  $\approx 5$  Hz. Such neural network showed patterns of activity very different from the weakly coupled networks inspected above, Figure 11. In particular, large number of highly correlated, synchronously locked firings of many neurons were evident in this network. Likewise, our Bayesian algorithm was not able to identify the true connectivity matrix correctly, Figure 11.

On the other hand, our inference algorithm showed significant robustness to deviations of the actual data from our generative model. One important such deviation, which is likely to occur in the real experiments, is variation in the time-scales of EPSPs in different synapses. Up to now, all EPSP time-scales  $\tau_w$  were assumed to be the same in our inference algorithm as well as in the simulations. In Figure 12 we introduce additional variability in  $\tau_w$  from one neuron to another. Variability in  $\tau_w$  results in added variance in the estimates of the connectivity weights  $w_{ij}$  through  $\tau_w$  dependence of the scaling factor Eq.(25). Still, we found that such added variance was insignificant with  $\tau_w$  varying for up to 25% from neuron to neuron, Figure 12.

**4. Discussion.** In this paper we develop a Bayesian approach for inferring functional connectivity in a population of spiking neurons imaged with calcium imaging. While similar problem of inferring functional connectivity from a set of simultaneous spike-train recordings had been previously addressed for micro-electrode techniques [(Rigat et al., 2006),XXX], and the problem of inferring spikes of individual neurons from calcium imaging data had been addresses before [(Vogelstein et al., 2009),XXX], we are the first to combine these two approaches to solve the problem of inferring functional connectivity from calcium imaging data.

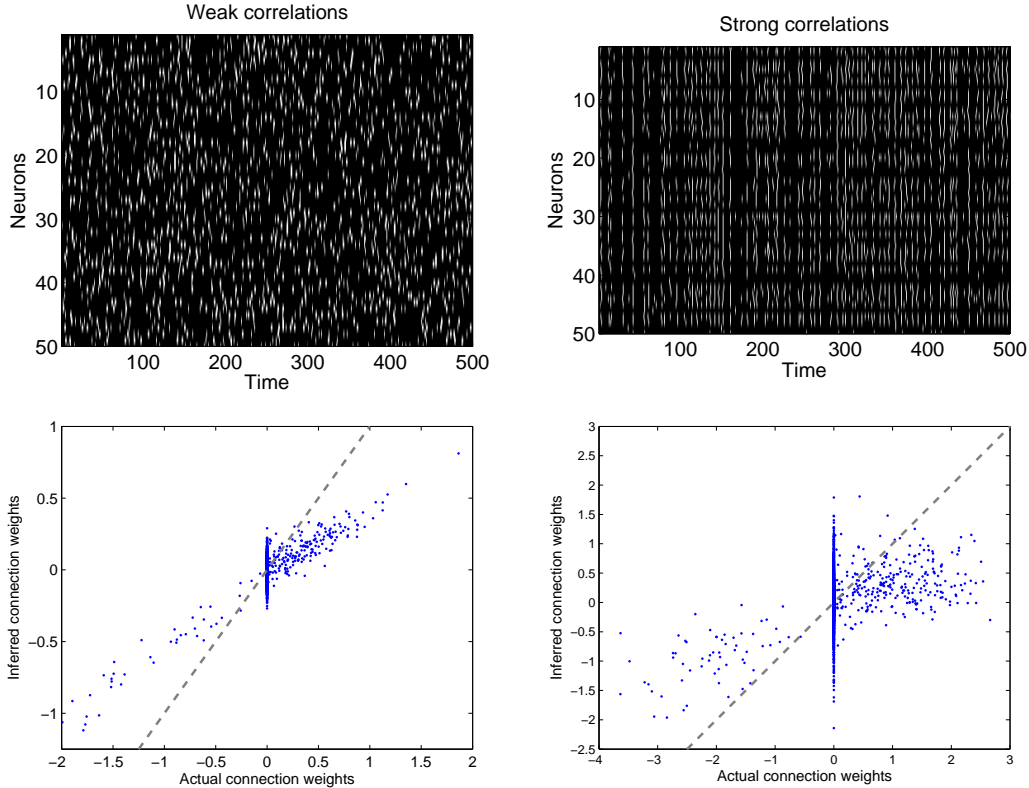


FIG 11. *Diverseness of observed neural activity patterns is required for functional connectivity to give access to the actual “anatomical” structure of the neural circuit. Here, 15 sec of simulated spike trains for a weakly coupled network (upper-left) and a network with strongly coupled component (upper-right) are shown. In weakly coupled network spikes are sufficiently uncorrelated to give access to all different neural activity patterns needed to properly estimate true weights  $\mathbf{w}_i$ . In strongly coupled case, many instances of highly synchronous locked firings are evident, thus preventing observation of sufficiently rich ensemble of activity patterns. Accordingly, GLM solution for the strongly coupled neural network (lower-right) does not represent the true connectivity of the circuit, even for the weakly coupled component. This is contrary to the weakly-coupled network (lower-left) where true connectivity is successfully obtained. Networks of  $N = 50$  neurons firing at  $\approx 5$  Hz and imaged for  $T = 600$  sec were used to produce this figure.*

Because calcium imaging, in principle, has capacity to image populations of cells containing  $\sim 1,000 - 100,000$  neurons, this opens the way for analysis of micro-circuitry in large and complete populations of neurons in neo-cortex or other brain areas.

«LIAM: Another discussion point: we'll want to discuss the work by fabio rigat specifically: <http://ba.stat.cmu.edu/journal/2006/vol01/issue04/rigat.pdf>, (Rigat et al., 2006)

they touched on a lot of similar themes: they stress the importance of the prior on the inference (they use a more complicated hierarchical prior for the network structure), they use a bernoulli glm as the foundation of their model, they develop a model to deal with misclassified spikes (they're dealing with noisy multielectrode recordings, but the issues are qualitatively similar to ours), and they end up using metropolis-within-gibbs as their main computational tool. definitely worth checking out if you haven't read this before; we should be careful to cite them where appropriate in the main text, and also discuss the overlap in the discussion.

YURly: I am not familiar with this work. J, if you can add something along the lines Liam wanted, please do, otherwise I put a cite to Rigat's paper above. »

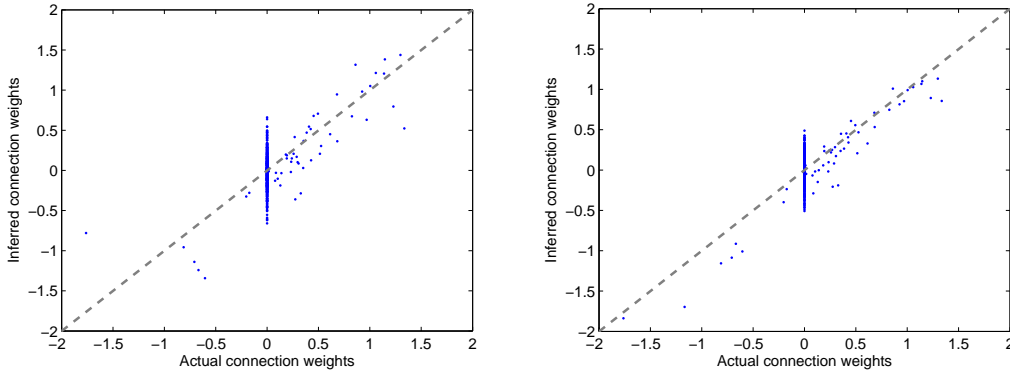


FIG 12. *Bayesian inference algorithm is robust to deviations of the data from our generative model. One such deviation, that should be expected in real data, is variability in the EPSP time courses from neuron to neuron, and possibly synapse to synapse. With up to 25% variability allowed in EPSP time scales  $\tau_w$  (right panel) our algorithm provided reconstructions of almost the same quality as when all  $\tau_w$  were the same (left panel). Simulation conditions are the same as in Figure 8.*

The main challenge in this problem is indirect nature of calcium imaging data, which provides only noisy, low-pass nonlinear filtered, temporally sub-sampled observations of spikes of individual neurons. In order to find connectivity parameters, in Bayesian settings, the hidden spike-train variables need to be integrated out. Obtaining a joint sample of unobserved spike trains, needed to compute relevant integrals, is very non-trivial problem given high dimensionality of the hidden state if number of neurons,  $N$ , is large. In particular, methods for analyzing calcium imaging data for single neurons, (Vogelstein et al., 2009), do not generalize well for this application. To solve this problem, in this paper we develop a new method for obtaining samples from a collection of coupled low-dimensional HMMs by embedding sampling chains of states from individual low-dimensional HMM within a Gibbs sampler that loops in a predefined order over different coupled HMMs. The functional connectivity matrix is then inferred by maximizing the expected value of posterior log-likelihood in EM framework. Exponential prior is used to enforce sparseness condition of the objective connectivity matrix, which allows to significantly reduce the minimal amount of data required for successful reconstruction.

By applying this method to observations of spontaneous activity in a simulated population of neurons, we can efficiently infer the functional connectivity matrix from only  $\sim 10$  min of simulated calcium imaging data (c.f Figure 9, 10). While embedded-chain-within-Gibbs methods leads to exact locally MAP estimate, under reasonable calcium imaging conditions we find that significant simplification is possible, where the posterior distribution may be assumed to approximately factorize,  $P(\mathbf{X}|\mathbf{F}; \theta) \approx \prod P(X_i|F_i; \tilde{\theta}_i)$ . This allows obtaining samples of joint spike trains  $\mathbf{X}$  much more easily and in parallel. Since the maximization procedure in EM also can be straightforwardly parallelized, thanks to special structure of the posterior likelihood, the entire inference method can be easily implemented as a highly parallelized application, offering significant savings in data-processing time. If calculations are performed on a large high-performance cluster, reconstruction of the connectivity matrix from  $\sim 10$  minutes of calcium imaging data can be performed nearly in real time, by solving each neuron on a separate node and utilizing only about 10 minutes of computational time per each node. This is an important virtue of our method.

Our method allows to measure functional connectivity conditioned on the spike trains of



all observed neurons, i.e.,  $(\mathbf{n}_1, \mathbf{n}_2 | \mathbf{n}_3, \dots, \mathbf{n}_N)$  ( $?$ ;  $?$ ;  $?$ ;  $?$ ;  $?$ ). This differs significantly from previous works [XXX], which naively defined functional connectivity as a function of spike trains of only two neurons,  $(\mathbf{n}_i, \mathbf{n}_j)$  - correlation coefficient, lagged cross-correlation, transfer entropy, or Granger causality. Since these measures explicitly ignore the spike trains of all other neurons, they suffer from the problems related to “third-neuron-mediated-interactions”. Specifically, if neuron  $i$  and neuron  $j$  both are strongly connected to third neuron  $k$ , such naive measures may report strong functional connection between neurons  $i$  and  $j$ , even in the presence of observations of neuron  $k$ . Our method has added power of resolving such mediated interactions, or “explaining away”: if correlation between neuron  $i$  and neuron  $j$  may be successfully modeled by functional connection with the third neuron  $k$ , our method will “explain away” such correlation, and assign to neurons  $i$  and  $j$  functional connection weight zero. We show that under certain condition (weak correlation among spike trains, c.f. Figure 6) our method allows reconstructing true, “anatomical”, connectivity matrix for the population of neurons solely from the activity data. At the same time, we demonstrate that under certain conditions such reconstruction from activity data alone may fail: if the spike trains are strongly correlated, functional connectivity matrix may not correspond to the true connectivity of the population even when all neurons are observed (c.f. Figure 11). Such failure can be explained by inability of monitoring neural activity in strongly correlated spike trains to properly sample the space of all activity patterns, necessary to reliably constrain  $\mathbf{w}$ .

In the view of these achievements and failures, a number of possible improvements of our method can be proposed. One of the biggest challenges for inferring neural connectivity from functional data is the presence of so called hidden inputs from unobserved neurons [XXX]. Since it is typically impossible to expect that activity of all neurons in a closed neural circuit can be monitored, such hidden inputs should be always anticipated in the real imaging data. Correlations in hidden inputs are capable of successfully mimicking functional connections among different observed neurons [XXX], thus presenting a substantial challenge for estimating neural circuit’s connectivity from activity observations alone. Developing methods to cope with such hidden inputs is currently area of active research ( $?$ ;  $?$ ). Incorporating these features into our model is an important direction for future work. Along with investigation of ways to combat the effect of unobserved neurons, we have considered several other potential directions for future improvements of our method. Incorporating photo-stimulation to activate or deactivate individual neurons or their sub-populations may be used to significantly increase statistical power of a given set of observations. Especially, such external probes of neural network may be helpful in the case where the natural activity of a circuit results in strongly correlated firing patterns [Rafa?]. Although naturally observed behavior may not allow reliable determination of circuit’s connectivity matrix, by utilizing external stimulation a sufficiently rich sample of activity patterns may be collected, and true anatomical structure of the neural circuit may be inferred. Developing the optimal sequences of artificial stimuli and their implementation in the actual experiments are other important directions for future work.

Furthermore, improvements of the algorithms for faster sampling spike trains from calcium imaging data, as well as for faster log-likelihood maximization may be possible [fast-filter?]. In particular, improvement in the spike-sampling algorithms for explicitly taking into account Poisson statistics of the spike counts in time-bins with large width,  $\Delta$ , rather than Bernoulli distribution used in this work, will be interesting. Modifications of our generative model allowing to deal with fluorescent signal non-stationarities, e.g. due to dye bleaching, and complicated effects in the dynamics of calcium concentration during spikes will be important

to reliably apply our method to real imaging data. Finally, a fully Bayesian algorithm for estimating the posterior distributions of all the parameters, as opposed to only finding the MAP estimate, is of great interest. Such fully-Bayesian extension is conceptually simple: we just need to extend this work’s Gibbs sampler to additionally sample from  $\theta$  given the spike trains  $\mathbf{X}$ . Since we already have a method for drawing the spike trains  $\mathbf{X}$  given  $\theta$  and  $\mathbf{F}$ , with such additional sampler we may obtain samples from  $P(\mathbf{X}, \theta | \mathbf{F})$  simply by sampling from  $\mathbf{X} \sim P(\mathbf{X} | \theta, \mathbf{F})$  and  $\theta \sim P(\theta | \mathbf{X})$  within Gibbs sampling procedure. Sampling from the posteriors  $P(\theta | \mathbf{X})$  in the GLM setting is tractable using hybrid Monte Carlo methods, since all the posteriors are log-concave (Ishwaran, 1999; Gamerman, 1997; Gamerman, 1998; Ahmadian et al., 2009).

All these advances are currently being pursued.

**Acknowledgements.** The authors would like to acknowledge Rafael Yuste, Brendon O. Watson, Adam Packer, Tanya Sippy, Tom Mrsic-Flogel and Vincent Bonin for data and helpful discussions.

## References.

- Abeles, M. (1991). *Corticonics*. Cambridge University Press.
- Ahmadian, Y., Pillow, J., and Paninski, L. (2009). Efficient Markov Chain Monte Carlo methods for decoding population spike trains. *Under review, Neural Computation*.
- Andrieu, C., Doucet, A., and Holenstein, A. (2007). Particle markov chain monte carlo. *Working paper*.
- Bickel, P., Li, B., and Bengtsson, T. (2008). Sharp failure rates for the bootstrap particle filter in high dimensions. In Clarke, B. and Ghosal, S., editors, *Pushing the Limits of Contemporary Statistics: Contributions in Honor of Jayanta K. Ghosh*, pages 318–329. IMS.
- Binzegger, T., Douglas, R. J., and Martin, K. A. C. (2004). A Quantitative Map of the Circuit of Cat Primary Visual Cortex. *J. Neurosci.*, 24(39):8441–8453.
- Boyd, S. and Vandenberghe, L. (2004). *Convex Optimization*. Oxford University Press.
- Braitenberg, V. and Schuz, A. (1998). *Cortex: statistics and geometry of neuronal connectivity*. Springer, Berlin.
- Brenowitz, S. D. and Regehr, W. G. (2007). Reliability and heterogeneity of calcium signaling at single presynaptic boutons of cerebellar granule cells. *J Neurosci*, 27(30):7888–7898.
- Briggman, K. L. and Denk, W. (2006). Towards neural circuit reconstruction with volume electron microscopy techniques. *Current Opinions in Neurobiology*, 16:562.
- Brillinger, D. (1988). Maximum likelihood analysis of spike trains of interacting nerve cells. *Biological Cybernetics*, 59:189–200.
- Brillinger, D. (1992). Nerve cell spike train data analysis: a progression of technique. *Journal of the American Statistical Association*, 87:260–271.
- Buhl, E., Halasy, K., and Somogyi, P. (1994). Diverse sources of hippocampal unitary inhibitory postynaptic potentials and the number of synaptic release sites. *Nature*, 368:823–828.
- Candes, E. J. and Romberg, J. (2005). Practical signal recovery from random projections.
- Chornoboy, E., Schramm, L., and Karr, A. (1988). Maximum likelihood identification of neural point process systems. *Biological Cybernetics*, 59:265–275.
- Dempster, A., Laird, N., and Rubin, D. (1977). Maximum likelihood from incomplete data via the EM algorithm. *Journal Royal Stat. Soc., Series B*, 39:1–38.

- Djurisic, M., Antic, S., Chen, W. R., and Zecevic, D. (2004). Voltage imaging from dendrites of mitral cells: EPSP attenuation and spike trigger zones. *J. Neurosci.*, 24(30):6703–6714.
- Donoho, D. and Elad, M. (2003). Optimally sparse representation in general (nonorthogonal) dictionaries via  $L^1$  minimization. *PNAS*, 100:2197–2202.
- Doucet, A., de Freitas, N., and N., G. (2001). *Sequential Monte Carlo in Practice*. Springer.
- Doucet, A., Godsill, S., and Andrieu, C. (2000). On sequential Monte Carlo sampling methods for Bayesian filtering. *Statistics and Computing*, 10:197–208.
- Escola, S. and Paninski, L. (2008). Hidden Markov models applied toward the inference of neural states and the improved estimation of linear receptive fields. *Under review, Neural Computation*.
- Feldmeyer, D., Egger, V., Lubke, J., and Sakmann, B. (1999). Reliable synaptic connections between pairs of excitatory layer 4 neurones within a single “barrel” of developing rat somatosensory cortex. *J Physiol*, 521 Pt 1:169–90.
- Feldmeyer, D. and Sakmann, B. (2000). Synaptic efficacy and reliability of excitatory connections between the principal neurones of the input (layer 4) and output layer (layer 5) of the neocortex. *J Physiol*, 525:31–9.
- Gamerman, D. (1997). Sampling from the posterior distribution in generalized linear mixed models. *Statistics and Computing*, 7(1):57–68.
- Gamerman, D. (1998). Markov chain monte carlo for dynamic generalised linear models. *Biometrika*, 85(1):215–227.
- Godsill, S., Doucet, A., and West, M. (2004). Monte Carlo smoothing for non-linear time series. *Journal of the American Statistical Association*, 99:156–168.
- Gomez-Urquijo, S. M., Reblet, C., Bueno-Lopez, J. L., and Gutierrez-Ibarluzea, I. (2000). Gabaergic neurons in the rabbit visual cortex: percentage, distribution and cortical projections. *Brain Res*, 862:171–9.
- Greenberg, D. S., Houweling, A. R., and Kerr, J. N. D. (2008). Population imaging of ongoing neuronal activity in the visual cortex of awake rats. *Nat Neurosci*.
- Gupta, A., Wang, Y., and Markram, H. (2000). Organizing principles for a diversity of gabaergic interneurons and synapses in the neocortex. *Science*, 287:273–8.
- Harris, K., Csicsvari, J., Hirase, H., Dragoi, G., and Buzsaki, G. (2003). Organization of cell assemblies in the hippocampus. *Nature*, 424:552–556.
- Hatsopoulos, N., Ojakangas, C., Paninski, L., and Donoghue, J. (1998). Information about movement direction obtained by synchronous activity of motor cortical neurons. *PNAS*, 95:15706–15711.
- Helmchen, F., Imoto, K., and Sakmann, B. (1996).  $Ca^{2+}$  buffering and action potential-evoked  $Ca^{2+}$  signaling in dendrites of pyramidal neurons. *Biophys J*, 70(2):1069–1081.
- Ishwaran, H. (1999). Applications of hybrid Monte Carlo to Bayesian generalized linear models: quasicomplete separation and neural networks. *Journal of Computational and Graphical Statistics*, 8:779–799.
- Iyer, V., Hoogland, T. M., and Saggau, P. (2006). Fast functional imaging of single neurons using random-access multiphoton (RAMP) microscopy. *J Neurophysiol*, 95(1):535–545.
- Koch, C. (1999). *Biophysics of Computation*. Oxford University Press.
- Kulkarni, J. and Paninski, L. (2007). Common-input models for multiple neural spike-train data. *Network: Computation in Neural Systems*, 18:375–407.
- Lefort, S., Tómm, C., Floyd Sarria, J.-C., and Petersen, C. C. H. (2009). The excitatory neuronal network of the c2 barrel column in mouse primary somatosensory cortex. *Neuron*, 61:301–16.

- Li, K. and Duan, N. (1989). Regression analysis under link violation. *Annals of Statistics*, 17:1009–1052.
- Litke, A., Bezayiff, N., Chichilnisky, E., Cunningham, W., Dabrowski, W., Grillo, A., Grivich, M., Grybos, P., Hottowy, P., Kachiguine, S., Kalmar, R., Mathieson, K., Petrusca, D., Rahman, M., and Sher, A. (2004). What does the eye tell the brain? development of a system for the large scale recording of retinal output activity. *IEEE Trans Nucl Sci*, pages 1434–1440.
- Livet, J., Weissman, T., Kang, H., Draft, R., Lu, J., Bennis, R., Sanes, J., and Lichtman, J. (2007). Transgenic strategies for combinatorial expression of fluorescent proteins in the nervous system. *Nature*, 450:56–62.
- Luczak, A., Bartho, P., Marguet, S., Buzsaki, G., and Harris, K. (2007). Sequential structure of neocortical spontaneous activity in vivo. *PNAS*, 104:347–352.
- McLachlan, G. and Krishnan, T. (1996). *The EM Algorithm and Extensions*. Wiley-Interscience.
- Micheva, K. and Smith, S. (2007). Array tomography: A new tool for imaging the molecular architecture and ultrastructure of neural circuits. *Neuron*, 55:25–36.
- Mishchenko, Y. (2009). Strategies for identifying exact structure of neural circuits with broad light microscopy connectivity probes. *Preprint*: <http://precedings.nature.com/documents/2669/version/2>.
- Mishchenko, Y., Spacek, J., Mendenhall, J., Chklovskii, D., and Harris, K. M. (2009). Reconstruction of hippocampal cal neuropil at nanometer resolution reveals disordered packing of processes and dependence of synaptic connectivity on local environment and dendritic caliber. *Preprint*: <http://precedings.nature.com/documents/2669/version/2>.
- Neal, R., Beal, M., and Roweis, S. (2003). Inferring state sequences for non-linear systems with embedded hidden Markov models. *NIPS*, 16.
- Ng, A. (2004). Feature selection,  $L_1$  vs.  $L_2$  regularization, and rotational invariance. *ICML*, 21.
- Nguyen, Q. T., Callamaras, N., Hsieh, C., and Parker, I. (2001). Construction of a two-photon microscope for video-rate  $\text{Ca}^{2+}$  imaging. *Cell Calcium*, 30(6):383–393.
- Nykamp, D. (2007). A mathematical framework for inferring connectivity in probabilistic neuronal networks. *Mathematical Biosciences*, 205:204–251.
- Paninski, L. (2004). Maximum likelihood estimation of cascade point-process neural encoding models. *Network: Computation in Neural Systems*, 15:243–262.
- Paninski, L., Fellows, M., Shoham, S., Hatsopoulos, N., and Donoghue, J. (2004). Superlinear population encoding of dynamic hand trajectory in primary motor cortex. *J. Neurosci.*, 24:8551–8561.
- Petersen, C. C. and Sakmann, B. (2000). The excitatory neuronal network of rat layer 4 barrel cortex. *J Neurosci*, 20(20):7579–86.
- Petrusca, D., Grivich, M. I., Sher, A., Field, G. D., Gauthier, J. L., Greschner, M., Shlens, J., Chichilnisky, E. J., and Litke, A. M. (2007). Identification and characterization of a Y-like primate retinal ganglion cell type. *J. Neurosci.*, 27(41):11019–11027.
- Pillow, J., Shlens, J., Paninski, L., Sher, A., Litke, A., Chichilnisky, E., and Simoncelli, E. (2008). Spatiotemporal correlations and visual signaling in a complete neuronal population. *Nature*, 454:995–999.
- Plesser, H. and Gerstner, W. (2000). Noise in integrate-and-fire neurons: From stochastic input to escape rates. *Neural Computation*, 12:367–384.
- Rabiner, L. (1989). A tutorial on hidden Markov models and selected applications in speech

- recognition. *Proceedings of the IEEE*, 77:257–286.
- Ramon y Cajal, S. (1904). *La Textura del Sistema Nerviosa del Hombre y los Vertebrados*. Moya.
- Ramon y Cajal, S. (1923). *Recuerdos de mi vida: Historia de mi labor cientifica*. Alianza Editorial.
- Reddy, G., Kelleher, K., Fink, R., and Saggau, P. (2008). Three-dimensional random access multiphoton microscopy for functional imaging of neuronal activity. *Nature Neuroscience*, 11(6):713–720.
- Reddy, G. D. and Saggau, P. (2005). Fast three-dimensional laser scanning scheme using acousto-optic deflectors. *J Biomed Opt*, 10(6):064038.
- Reyes, A., Lujan, R., Rozov, A., Burnashev, N., Somogyi, P., and Sakmann, B. (1998). Target-cell-specific facilitation and depression in neocortical circuits. *Nat Neurosci*, 1:279–285.
- Rigat, F., de Gunst, M., and van Pelt, J. (2006). Bayesian modelling and analysis of spatio-temporal neuronal networks. *Bayesian Analysis*, 1:733–764.
- Robert, C. and Casella, G. (2005). *Monte Carlo Statistical Methods*. Springer.
- Salome, R., Kremer, Y., Dieudonne, S., Leger, J.-F., Krichevsky, O., Wyart, C., Chatenay, D., and Bourdieu, L. (2006). Ultrafast random-access scanning in two-photon microscopy using acousto-optic deflectors. *Journal of Neuroscience Methods*, 154(1-2):161–174.
- Santhanam, G., Ryu, S. I., Yu, B. M., Afshar, A., and Shenoy, K. V. (2006). A high-performance brain-computer interface. *Nature*, 442:195–198.
- Sayer, R. J., Friedlander, M. J., and Redman, S. J. (1990). The time course and amplitude of epsps evoked at synapses between pairs of ca3/ca1 neurons in the hippocampal slice. *J. Neurosci.*, 10:826–36.
- Segev, R., Goodhouse, J., Puchalla, J., and Berry, M. (2004). Recording spikes from a large fraction of the ganglion cells in a retinal patch. *Nature Neuroscience*, 7:1154–1161.
- Shumway, R. and Stoffer, D. (2006). *Time Series Analysis and Its Applications*. Springer.
- Song, S., Sjostrom, P. J., Reigl, M., Nelson, S., and Chklovskii, D. B. (2005). Highly nonrandom features of synaptic connectivity in local cortical circuits. *PLoS Biology*, 3:e68.
- Stein, R. B., Weber, D. J., Aoyagi, Y., Prochazka, A., Wagenaar, J. B. M., Shoham, S., and Normann, R. A. (2004). Coding of position by simultaneously recorded sensory neurones in the cat dorsal root ganglion. *J Physiol (Lond)*, 560(3):883–896.
- Stevenson, I., Rebesco, J., Hatsopoulos, N., Haga, Z., Miller, L., and Koerding, K. (2008). Inferring network structure from spikes. *Statistical Analysis of Neural Data meeting*.
- Stevenson, I. H., Rebesco, J. M., Hatsopoulos, N. G., Haga, Z., Miller, L. E., and Kording, K. P. (2009). Bayesian inference of functional connectivity and network structure from spikes. *IEEE Trans. Neural Systems and Rehab.*, 17:203–13.
- Stosiek, C., Garaschuk, O., Holthoff, K., and Konnerth, A. (2003). In vivo two-photon calcium imaging of neuronal networks. *Proceedings of The National Academy Of Sciences Of The United States Of America*, 100(12):7319–7324.
- Thompson, A., Girdlestone, D., and West, D. (1988). Voltage-dependent currents prolong single-axon postsynaptic potentials in layer III pyramidal neurons in rat neocortical slices. *J Neurophysiol*, 60:1896–1907.
- Tibshirani, R. (1996). Regression shrinkage and selection via the lasso. *Journal of the Royal Statistical Society. Series B*, 58:267–288.
- Tipping, M. (2001). Sparse Bayesian learning and the relevance vector machine. *Journal of Machine Learning Research*, 1:211–244.
- Truccolo, W., Eden, U., Fellows, M., Donoghue, J., and Brown, E. (2005). A point process

- framework for relating neural spiking activity to spiking history, neural ensemble and extrinsic covariate effects. *Journal of Neurophysiology*, 93:1074–1089.
- Tsien, R. Y. (1989). Fluorescent probes of cell signaling. *Ann. Rev. Neurosci.*, 12:227–253.
- Vidne, M., Kulkarni, J., Ahmadian, Y., Pillow, J., Shlens, J., Chichilnisky, E., Simoncelli, E., and Paninski, L. (2009). Inferring functional connectivity in an ensemble of retinal ganglion cells sharing a common input. *COSYNE*.
- Vogelstein, J. T., Watson, B. O., Packer, A. M., Yuste, R., Jedynak, B., and Paninski, L. (2009). Spike inference from calcium imaging using sequential monte carlo methods. *Preprint*.
- Wallace, D., zum Alten Borgloh, S., Astori, S., Yang, Y., Bausen, M., K  
"ugler, S., Palmer, A., Tsien, R., Sprengel, R., Kerr, J., Denk, W., and Hasan, M. (2008). Single-spike detection in vitro and in vivo with a genetic Ca<sup>2+</sup> sensor. *Nature methods*, 5(9):797–804.
- Yaksi, E. and Friedrich, R. W. (2006). Reconstruction of firing rate changes across neuronal populations by temporally deconvolved Ca<sup>2+</sup> imaging. *Nature Methods*, 3(5):377–383.
- Yasuda, R., Nimchinsky, E. A., Scheuss, V., Pologruto, T. A., Oertner, T. G., Sabatini, B. L., and Svoboda, K. (2004). Imaging calcium concentration dynamics in small neuronal compartments. *Sci STKE*, 219:p15.
- Yuste, R., Konnerth, A., Masters, B., et al. (2006). *Imaging in Neuroscience and Development, A Laboratory Manual*.